



NAVAL POSTGRADUATE SCHOOL

MONTEREY, CALIFORNIA

DISSERTATION

**REAL-TIME TERAHERTZ IMAGING USING A
QUANTUM CASCADE LASER AND UNCOOLED
MICROBOLOMETER FOCAL PLANE ARRAY**

by

Barry Neal Behnken

June 2008

Dissertation Supervisor:

Gamani Karunasiri

Approved for public release; distribution is unlimited

THIS PAGE INTENTIONALLY LEFT BLANK

REPORT DOCUMENTATION PAGE			<i>Form Approved OMB No. 0704-0188</i>	
Public reporting burden for this collection of information is estimated to average 1 hour per response, including the time for reviewing instruction, searching existing data sources, gathering and maintaining the data needed, and completing and reviewing the collection of information. Send comments regarding this burden estimate or any other aspect of this collection of information, including suggestions for reducing this burden, to Washington headquarters Services, Directorate for Information Operations and Reports, 1215 Jefferson Davis Highway, Suite 1204, Arlington, VA 22202-4302, and to the Office of Management and Budget, Paperwork Reduction Project (0704-0188) Washington DC 20503.				
1. AGENCY USE ONLY (Leave blank)		2. REPORT DATE June 2008	3. REPORT TYPE AND DATES COVERED Dissertation	
4. TITLE AND SUBTITLE: Real-Time Terahertz Imaging using a Quantum Cascade Laser and Uncooled Microbolometer Focal Plane Array			5. FUNDING NUMBERS	
6. AUTHOR(S) Barry Neal Behnken			8. PERFORMING ORGANIZATION REPORT NUMBER	
7. PERFORMING ORGANIZATION NAME(S) AND ADDRESS(ES) Naval Postgraduate School Monterey, CA 93943-5000			10. SPONSORING / MONITORING AGENCY REPORT NUMBER	
9. SPONSORING / MONITORING AGENCY NAME(S) AND ADDRESS(ES) N/A				
11. SUPPLEMENTARY NOTES The views expressed in this thesis are those of the author and do not reflect the official policy or position of the Department of Defense or the U.S. Government.				
12a. DISTRIBUTION / AVAILABILITY STATEMENT Approved for public release; distribution is unlimited.			12b. DISTRIBUTION CODE	
13. ABSTRACT (maximum 200 words) Real-time imaging in the terahertz (THz) spectral range was achieved using an uncooled, 160×120 pixel infrared microbolometer camera and a milliwatt-scale quantum cascade laser (QCL). By replacing the camera's original focusing optics with a Tsurupica-based lens and minimizing diffraction effects incurred by the QCL output beam, an imaging scheme was developed in which the camera's focal plane array successfully detected wavelengths that are more than an order of magnitude longer than those for which the system is designed. Moreover, the incorporation of parabolic reflecting optics yielded a capability to produce high-resolution images of objects placed within the beam path. Despite the low laser powers employed, this scheme allows high-contrast imaging of various objects concealed by a wide range of nonmetallic materials—confirming the suitability of this technology for homeland security screening applications. Furthermore, the identification of relatively obscure security features in British currency notes suggests that Terahertz imaging could serve a future role as a detection mechanism against assorted counterfeiting practices. An extensive comparative analysis of experimental data produced using two QCLs (resonating at 2.8 and 3.6 THz) provides additional insight into the physics underlying these results, and suggests methods by which this imaging technology could be further improved.				
14. SUBJECT TERMS THz, terahertz, real-time, microbolometer, uncooled, QCL, quantum cascade laser, imaging, detection, camera, focal plane array, Tsurupica, NETD, NEP, vanadium oxide, silicon nitride.			15. NUMBER OF PAGES 101	
			16. PRICE CODE	
17. SECURITY CLASSIFICATION OF REPORT Unclassified	18. SECURITY CLASSIFICATION OF THIS PAGE Unclassified	19. SECURITY CLASSIFICATION OF ABSTRACT Unclassified	20. LIMITATION OF ABSTRACT UU	

NSN 7540-01-280-5500

Standard Form 298 (Rev. 2-89)
Prescribed by ANSI Std. Z39-18

THIS PAGE INTENTIONALLY LEFT BLANK

Approved for public release; distribution is unlimited

**REAL-TIME TERAHERTZ IMAGING USING A QUANTUM CASCADE LASER
AND UNCOOLED MICROBOLOMETER FOCAL PLANE ARRAY**

Barry N. Behnken
Major, United States Air Force
B.S., Applied Physics, United States Air Force Academy, 1993
M.S., Engineering Physics, Air Force Institute of Technology, 1999

Submitted in partial fulfillment of the
requirements for the degree of

DOCTOR OF PHILOSOPHY IN PHYSICS

from the

**NAVAL POSTGRADUATE SCHOOL
June 2008**

Author:

Barry N. Behnken

Approved by:

Gamani Karunasiri
Professor of Physics
Dissertation Supervisor

William Colson
Distinguished Professor of
Physics

Andrés Larraza
Associate Professor of Physics

Danielle Chamberlin
Senior Scientist
Agilent Laboratories

Jose Sinibaldi
Research Associate Professor of
Mechanical Engineering

Approved by:

James Luscombe, Chair, Department of Physics

Approved by:

Douglas Moses, Associate Provost for Academic Affairs

THIS PAGE INTENTIONALLY LEFT BLANK

ABSTRACT

Real-time imaging in the terahertz (THz) spectral range was achieved using an uncooled, 160×120 pixel infrared microbolometer camera and a milliwatt-scale quantum cascade laser (QCL). By replacing the camera's original focusing optics with a Tsurupica-based lens and minimizing diffraction effects incurred by the QCL output beam, an imaging scheme was developed in which the camera's focal plane array successfully detected wavelengths that are more than an order of magnitude longer than those for which the system is designed. Moreover, the incorporation of parabolic reflecting optics yielded a capability to produce high-resolution images of objects placed within the beam path. Despite the low laser powers employed, this scheme allows high-contrast imaging of various objects concealed by a wide range of nonmetallic materials—confirming the suitability of this technology for homeland security screening applications. Furthermore, the identification of relatively obscure security features in British currency notes suggests that Terahertz imaging could serve a future role as a detection mechanism against assorted counterfeiting practices. An extensive comparative analysis of experimental data produced using two QCLs (resonating at 2.8 and 3.6 THz) provides additional insight into the physics underlying these results, and suggests methods by which this imaging technology could be further improved.

THIS PAGE INTENTIONALLY LEFT BLANK

TABLE OF CONTENTS

I.	INTRODUCTION.....	1
II.	BACKGROUND	3
III.	THE SOURCE: QUANTUM CASCADE LASER (QCL).....	7
	A. QCL THEORY/BACKGROUND	7
	B. TERAHERTZ QCL OPERATION.....	13
IV.	THE SENSOR: MICROBOLOMETER FPA.....	17
	A. MICROBOLOMETER THEORY/ BACKGROUND	17
	B. NOISE ANALYSIS.....	26
V.	EXPERIMENTAL PROCEDURES	31
	A. IMAGING ARRANGEMENT	31
	B. FTIR ANALYSIS.....	38
	C. FPA SENSITIVITY	40
	D. IMPACT OF QCL TEMPERATURE ON IMAGING RESULTS.....	41
VI.	IMAGING RESULTS	47
	A. IMAGING AT 2.7 THz	48
	B. IMAGING AT 3.6 THz	53
	C. IMAGING AT 0.7-3.0 THz USING INTRACAVITY DFG	58
VII.	POTENTIAL IMPROVEMENTS TO THE IMAGING SYSTEM.....	63
	A. DIFFRACTION EFFECTS	63
	B. OUTPUT POWER.....	64
	C. COMPACTNESS.....	67
	D. TERAHERTZ-TUNED MICROBOLOMETER DESIGN	69
	E. RECENT IMPROVEMENTS IN MICROBOLOMETER-BASED DETECTOR TECHNOLOGY	71
VIII.	CONCLUSIONS	73
	LIST OF REFERENCES.....	75
	INITIAL DISTRIBUTION LIST	81

THIS PAGE INTENTIONALLY LEFT BLANK

LIST OF FIGURES

Fig. 1. Terahertz radiation (“T-rays”) with respect to rest of the electromagnetic spectrum (from [43]).....	3
Fig. 2. Methods of producing terahertz radiation. “DFG” refers to difference-frequency generation, a technique which is used to generate the THz beam studied by the author during a late collaboration effort with Stanford University researchers. (from [46])	7
Fig. 3. Band structure of a conventional three-level QCL, in which depopulation from the discrete lower laser level is via optical-phonon interactions (from [52]).....	9
Fig. 4. Band structure of a bound-to-continuum quantum cascade laser, characteristic of the device used to produce terahertz radiation in the present research (from [53]).....	12
Fig. 5. Schematic of quantum cascade laser used in imaging experiments. The active region of the laser consists of 120 periods of GaAs/AlGaAs quantum wells (after [53]).....	13
Fig. 6. I-V data for the 3.6-THz QCL, operated under various duty cycles. Dynamic impedance of the device is given by the reciprocal of the slope of the linear region of the curves.....	15
Fig. 7. I-V data of the 3.6-THz QCL, operated under 10% duty cycle, at various cryostat temperatures. The I-V data set labeled as “10-20 K” was collected with cold head thermostat set to 10 K; however, closed-cycle refrigeration was not sufficiently robust to prevent an elevation of temperature (by Joule heating), to as high as 20 K, at higher bias currents.	15
Fig. 8. Infrared image of the author, taken under conventional operation of the microbolometer camera used in this study (without optical modifications)....	18
Fig. 9. The imaging system used in the present research: Infrared Solutions IR-160 infrared microbolometer camera (from [54]).....	18
Fig. 10. The imaging system used in the present research: Infrared Solutions IR-160 infrared microbolometer camera (from [54]).....	19
Fig. 11. Schematic of a typical MEMS-fabricated microbolometer pixel. Primary architectural elements (support arms and upper pixel membrane) are comprised of Si_3N_4 . VO_x is layered upon Si_3N_4 membrane to provide the pixel with a high TCR response to incident radiation. SiO_2 is used as a sacrificial layer to provide spatial separation of the membrane from the substrate layer, thus ensuring that the only thermal conduction allowed is that from the membrane through the support arms (from [55]).....	20
Fig. 12. Planck radiation curve for a 300 K (room temperature) blackbody, showing spectral irradiance as a function of frequency. The area of the left and right shaded regions represents total power density associated with the 1-5 THz and 21.4-37.5 THz (8-14 μm) spectral band, respectively.	27
Fig. 13. QCL assembly used in initial imaging trials. QCL was mounted such that beam is emitted horizontally onto a flat mirror, then further reflected off of a	

parabolic mirror before exiting the chamber through a Tsurupica-based window (from [37]).....	32
Fig. 14. Still images of video clips (taken by a frame grabber at 18 Hz frame rate) of real-time terahertz detection using a 3.6-THz QCL and IR-160 microbolometer FPA. (a) Unobstructed beam. (b) Beam with a metal pen passing between beam source and detector. (c) Beam obstructed by one sheet of bond paper. (d) Beam obstructed by two sheets of paper.	33
Fig. 15. Measured transmittance of a Tsurupica window as a function of frequency in the terahertz regime.	35
Fig. 16. Second QCL assembly design used within cryostat (with external cold head housing removed). Laser element is affixed to a copper carrier to facilitate transfer of thermal energy away from the laser. When lasing, beam is emitted outward, from QCL edge, along direction of red arrow (inset).	36
Fig. 17. Optical configuration used in most recent series of terahertz imaging experiments. Lower and upper mirrors (50.8 mm and 101.6 mm focal length, respectively) were used to focus and steer the terahertz beam emerging from the Tsurupica window of the cryostat to the focal plane array of the microbolometer (beam path is illustrated by red arrow).	37
Fig. 18. Optical configuration used to conduct FTIR measurements of 3.6-THz QCL beam. A gold-coated, f/1 parabolic reflector was used with a silver-coated parabolic reflector for focusing and directing the beam into the external port of the FTIR spectrometer. Measurements were taken with the QCL operating under an applied bias of 1.6-1.7 A.	38
Fig. 19. Output power as a function of current for various duty cycles (D). Each data point was collected by FTIR spectroscopy using 16 scans at a resolution of 1 cm^{-1} and a mirror speed of 0.64 m/s.	39
Fig. 20. Measured voltage across the laser and normalized image intensity of the QCL, operated at 15% duty cycle, as a function of current. The image quality associated with specific levels of signal intensity is illustrated by the inset images, taken by microbolometer FPA, of an unobstructed beam at operating currents of 1.0 A, 1.3 A, 1.8 A, 2.1 A, and 2.2 A.	41
Fig. 21. Effects of duty cycle on laser performance: Signal intensity detected by FPA while operating QCL, at 300 kHz pulse rate and applied bias of 9.7-10.5 V, over extended period of time. (Cryostat set to 10 K.).....	42
Fig. 22. Effects of temperature on laser performance for various duty cycles (D): Signal intensity detected by FPA while operating QCL, at 300 kHz pulse rate and applied bias of 9.7-10.5 V, over extended period of time. (Cryostat set to 10 K.)	43
Fig. 23. Cryostat temperature changes arising from operation of the QCL at 20% duty cycle and applied bias of 10.4 V (1.7 A). Under these conditions, the cryostat reaches a steady-state temperature of 29 K after approximately eight minutes. Upon ceasing current flow to the laser, cryostat temperature drops at an approximate rate of 0.2 K/sec.	45
Fig. 24. Imaging of a small utility knife blade wrapped in opaque plastic tape. (a) Conventional digital photograph. Red dotted region represents	

	approximate area of illumination. (b) Single frame image of blade assembly illuminated with 2.7-THz QCL radiation and imaged with microbolometer camera. (c) Image generated by computationally averaging 50 individual frames. (d) Fifty-frame composite image, refined using MATLAB image processing utility software. Orphan particle is visible within red circle.....	49
Fig. 25.	Imaging of a large paper clip wrapped in opaque plastic tape. (a) Conventional digital photograph. Red dotted region represents approximate area of illumination. (b) Single frame image of blade assembly illuminated with 2.7-THz QCL radiation and imaged with microbolometer camera. (c) Image generated by computationally averaging 50 individual frames. (d) Fifty-frame composite image, refined using MATLAB image processing utility software.	50
Fig. 26.	Various objects, wrapped within two layers of opaque plastic tape, imaged using 2.7-THz QCL and microbolometer FPA. Upper images are conventional photographs taken with a compact digital camera; lower images are 50-frame averages of terahertz images enhanced with MATLAB noise reduction post-processing. (a, d). Dentist's pick. (b, e). Dissection scalpel with curved blade. (c, f). Plastic tie bent into a loop.	51
Fig. 27.	Still images of video clips (with post-processing filters applied) from imaging experiments conducted using microbolometer FPA and 2.7-THz QCL operated at a 300 kHz pulse repetition rate, 8% duty cycle, and applied bias of 1.0 A. All objects were wrapped in two layers of opaque plastic tape. (a) Steel utility blade. (b) Dentist's pick. (c) Large paperclip. (d) Plastic tie bent into the shape of a wire loop.	52
Fig. 28.	Still images of video clips (with post-processing filters applied) from imaging experiments conducted using microbolometer FPA and 3.6-THz QCL operated at a 300 kHz pulse repetition rate, 20% duty cycle, and applied bias of 1.9 A. (a) Steel utility blade obscured by two layers of opaque plastic tape. (b) Utility blade concealed with common bond paper. (c) Mylar [®] film cut in the shape of the Ironman Triathlon [®] "M-Dot" logo and enclosed by two layers of opaque plastic tape. (d) Finger of a black polyurethane glove containing an Allen wrench, which in turn is wrapped with a small swatch of opaque plastic tape.	54
Fig. 29.	Still images of video clips (with colorizing and post-processing filters applied) from imaging experiments conducted using microbolometer FPA and 3.6-THz QCL operated at a 300 kHz pulse repetition rate, 20% duty cycle, and applied bias of 1.9 A. (a) Steel utility blade obscured by a layer of Plexiglas. (b) mechanical pencil lead embedded in foam. (c) Watermark of President Abraham Lincoln from a U.S. \$5 bill (embedded video clip also includes imaging of plastic security thread). (d) "NPS" ("N" in still-frame image) written in number-two pencil, on a sheet of common bond paper.	56
Fig. 30.	£5 Great Britain Pound (GBP) note. (a) Watermark image of Queen Elizabeth II, as seen under illumination by forward-incident and rear-incident white	

light source (top-left and bottom-right corners, respectively). Only under the latter scheme is the watermark visible. (b) Terahertz imaging of watermark using microbolometer FPA and 3.6-THz QCL operated at a 300 kHz pulse repetition rate, 20% duty cycle, and applied bias of 1.9 A (with post-processing filters applied). (c) £5 security thread as seen under illumination by forward-incident and rear-incident white light source (top-left and bottom-right corners, respectively). (d) Terahertz imaging of security thread (using same operating parameters as in (b)). Notable in this animation is the elaborate *cross*-thread structure, a security feature which is relatively undetectable using white light sources.....57

Fig. 31. Three-dimensional intensity map of the Stanford OPO laser beam during production of 2.8 THz radiation, as measured by IR-160 focal plane array (without low-pass filter). Due to the frequency-mixing scheme, beam intensity is predominantly attributable to the two ~2 μm signal and idler beams.	60
Fig. 32. Colorized frame capture of IR-160 camera under illumination by 2.8 THz OPO beam (with Microtech lowpass terahertz filter included in beam path.).....	60
Fig. 33. FPA output from Thermoteknix Miricle 110K thermal imager, under illumination by 3.6 THz QCL output beam. The frame shown here makes use of the camera’s contour plotting feature, in which varying levels of signal intensity are represented by a range of colors from blue (high intensity) to red (low intensity).....	72

EXECUTIVE SUMMARY

Real-time imaging in the terahertz (THz) spectral range was achieved using an uncooled, 160×120 pixel infrared microbolometer camera and a milliwatt-scale quantum cascade laser (QCL). By replacing the camera's original focusing optics with a Tsurupica-based lens and minimizing diffraction effects incurred by the QCL output beam, an imaging scheme was developed in which the camera's focal plane array successfully detected wavelengths that are more than an order of magnitude longer than those for which the system is designed. Moreover, the incorporation of parabolic reflecting optics yielded a capability to produce high-resolution images of objects placed within the beam path. Noise equivalent temperature difference of the camera in the 1-5 THz frequency range was calculated to be at least 3 K, confirming the need for external terahertz illumination when imaging in this frequency regime. After evaluating the effects of various operating parameters on laser performance, the QCL was found to perform optimally at 1.9 A in pulsed mode with a 300 kHz repetition rate and 10-20% duty cycle. Despite the low average laser powers employed (0.4–1.4 mW), this scheme allows high-contrast imaging of various objects concealed by a wide range of nonmetallic materials—confirming the suitability of this technology for homeland security screening applications. Furthermore, the identification of relatively obscure security features in British currency notes suggests that terahertz imaging could serve a future role as a detection mechanism against assorted counterfeiting practices. An extensive comparative analysis of experimental data produced using two QCLs (resonating at 2.8 and 3.6 THz) provides additional insight into the physics underlying these results, and suggests methods by which this imaging technology could be further improved.

Throughout the course of this research, theoretical and experimental results were presented at a variety of scientific forums. The author presented various portions of this work at the 2007 American Physical Society Meeting, the 2007 SPIE Defense & Security Conference, the Ninth International Conference on Intersubband Transitions in Quantum Wells, SPIE Photonics West 2008, and as the keynote address of the 2008 Northern California Junior Sciences and Humanities Symposium. Scientific papers were published

in the proceedings of three of these symposia (*Proc. SPIE 6893*, *Proc. SPIE 6549*, and *Proc. 9th Int. Conf. on Intersubband Transitions in Quantum Wells*), as well as in the March 1, 2008 issue of *Optics Letters*. This research was also profiled in an article appearing in the April 2008 issue of *Laser Focus World*.

ACKNOWLEDGMENTS

To paraphrase Isaac Newton (to whom I am in no way, aside from rhetorical allusions, comparing myself), I have truly stood on the shoulders of giants while pursuing this dynamically winding, occasionally frustrating, and always exciting path of research. A word of forewarning: To fully acknowledge each person's contributions to my work and/or sanity, this section may be a bit longer than is typical. I owe great thanks to the following:

To my advisor, Professor Gamani Karunasiri, one of the kindest, most supportive, and luminous people I have known—for his wise and measured counsel, intellectual (and financial!) support, excellent instruction inside and outside of classrooms, and for entrusting me with the opportunity and responsibility to work with such complete independence on an area of research as rich and promising as the emerging field of terahertz imaging.

To Professors Andrés Larraza, William Colson, Jose Sinibaldi and Dr. Danielle Chamberlin, for agreeing to serve on my committee. I could never ask for a more brilliant and, yet, approachable assembly of PhD committee members. Over the past two years or so, each has made significant contributions to my development as a doctoral “apprentice,” and this counsel and guidance is very much appreciated. It is also important to note that this research likely would not even be possible, were it not for Professor Karunasiri's and Dr. Chamberlin's novel (and rather radical) idea to use microbolometers to detect radiation at wavelengths that are a full order of magnitude longer than those for which the camera is designed. Along those same lines, I would be remiss if I did not thank Dr. Chamberlin and Dr. Peter Robrish of Agilent Laboratories for generously providing the two quantum cascade lasers that constituted one half of the imaging system described in this thesis. Without those sources, NPS would be entirely incapable of conducting any form of terahertz experiments. I am confident they will continue to pay dividends for future GSEAS/PH students as well.

To NPS Physics Department Professors Luscombe, Armstead, Davis, and Walters, for the outstanding instruction they provided on thermal/statistical physics, electromagnetic theory, and Fourier/statistical optics during the coursework portion of my tenure here—subjects that figured very prominently into the research that followed. Each of these individuals exhibit a love and talent for teaching which is tremendously inspiring. As much as I value their instruction, however, I think I will more sorely miss each man’s unique personality, razor-sharp wit, and impressively droll sense of humor.

To Michelle Lowe and Kevin Buchanan, fellow students in the NPS sensors research group, who proved to be great collaborators and a solid sounding board for new ideas of experimental research.

To Sam Barone and George Jacksha, for providing superb (not to mention timely and responsive) technical support on the machining and engineering aspects of this research. In an attempt to continually improve the performance of this imaging system, we have made numerous in-house engineering changes to both the laser and thermal camera. With each new change, Sam and George were always quick to provide a tool/device/wisecrack (accompanied, without exception, with a smile). Aside from appreciating their help in making the “thing” (whatever it was at the time) do what it was supposed to do, I treasure the many conversations I’ve had with them both—mostly about topics completely unrelated to laser physics.

To my mother and my brother—for their support, friendship, and many great conversations. And to my father, whose memory still gives me great comfort.

To my children, who without fail buoyed my spirit when it was burdened with strain—and who always gave me a wonderful reason for a brief or extended study break. It is to them that this thesis is dedicated.

- To Nicole, who sweetly but with grave great concern insisted that I shouldn’t become a “doctor” because I’m much better at being a daddy.
- To Kyle, a boy of few words, whose smile, gesture, furrowed brow, outstretched offering, and/or occasional yell never failed to melt my concerns away.

And finally, and most importantly, to Yvonne—for her steadfast love, support, and clear thinking... especially when my own cluttered head wasn't working so well. I both appreciate and lament the sacrifices you have made while supporting my work. Thank you for always being there for me, and for your patience and understanding over the past three years.

THIS PAGE INTENTIONALLY LEFT BLANK

I. INTRODUCTION

A recent increase in homeland security concerns has precipitated a simultaneous demand for new imaging technologies. Of particular interest is the development of imaging systems that can quickly and efficiently detect concealed metal objects without posing health risks to humans. Owing to its unique spectral characteristics, radiation in the 0.3-10 terahertz (THz) spectral range has drawn recent attention as a new and potentially powerful medium for next-generation imaging technology [1]-[41].

Equipped with an appropriate illuminating source and sensor, terahertz imaging systems are capable of stand-off imaging of concealed objects and of human body tissue—particularly cancerous growths, which can elude x-ray based imaging detection [9]-[17]. Such detection agility is due to the fact that terahertz wavelengths are short enough to provide sub-millimeter resolution capability, yet are also long enough to penetrate most non-metallic materials [18]-[19]. At the same time, terahertz radiation is strongly reflected by nearly all metallic substances—providing a unique opportunity for high-contrast imaging of metal objects concealed in common materials such as fabric, paper, or plastic. This capability makes terahertz imaging a useful technology for identification of many dangerous or prohibited objects. Furthermore, many explosive materials absorb strongly in the terahertz spectral band—suggesting additional applications for stand-off spectroscopic analysis and identification of concealed explosives [20]-[22]. As an added benefit, the non-ionizing nature of terahertz radiation allows it to be used directly with humans without incurring the health hazards associated with other imaging technologies. For these reasons, terahertz technology holds promise as a multi-fold solution to what is likely the most pernicious homeland security issue today: fast, safe, and effective screening of passengers and their belongings at mass-transit accumulation points, and stand-off identification of explosive or otherwise hazardous materials.

In its present state, however, terahertz-based technology falls far short of supporting such grand applications. Currently, most terahertz imaging systems are based

on either antenna-coupled semiconductor detectors or cryogenically-cooled bolometers operating in the scan mode [1]-[4]. While successful, these techniques are disadvantaged by a lack of portability, slow response, the need for cryogenic cooling, and/or high expense. As a result, they are incapable of providing a complete solution to the imaging problem. A relatively new method of terahertz imaging involves a different approach: the use of microbolometer cameras. Because this technology is based upon temperature-driven changes in pixel resistivity that are produced by the absorption of incident photons (rather than electron-hole generation/recombination, as is used in most semiconductor-based photodetectors), the devices are not susceptible to thermal excitation and can be routinely operated at room temperature [42]. Furthermore, the relatively short thermal time constant (10 ms) of the microbolometer focal plane array (FPA) allows real-time imaging at television frame rates (30 Hz). Nearly all such cameras are designed and engineered for use in the infrared regime (typically 8-12 μm). Nevertheless, this dissertation reports the successful use of an optically-modified microbolometer system for imaging of quantum cascade laser (QCL) beams at 2.8 and 3.6 THz. Combined with theoretical calculations, the experimental data produced during these imaging trials strongly support the conclusion that this approach holds much promise as a viable imaging technology for future use in homeland security applications.

II. BACKGROUND

Given the extent to which scientists and engineers have successfully exploited the electromagnetic spectrum for technological purposes, it is perhaps surprising that a region as broad as the 0.3–10 THz frequency range (1.0–0.3 mm wavelength range) has remained largely untapped to date. Indeed, as is clear from Fig. 1, this range—which is often euphemistically referred to as the “terahertz gap”—is virtually the only portion of the spectrum between gamma rays and radio waves which has not found a wealth of everyday uses in contemporary society.

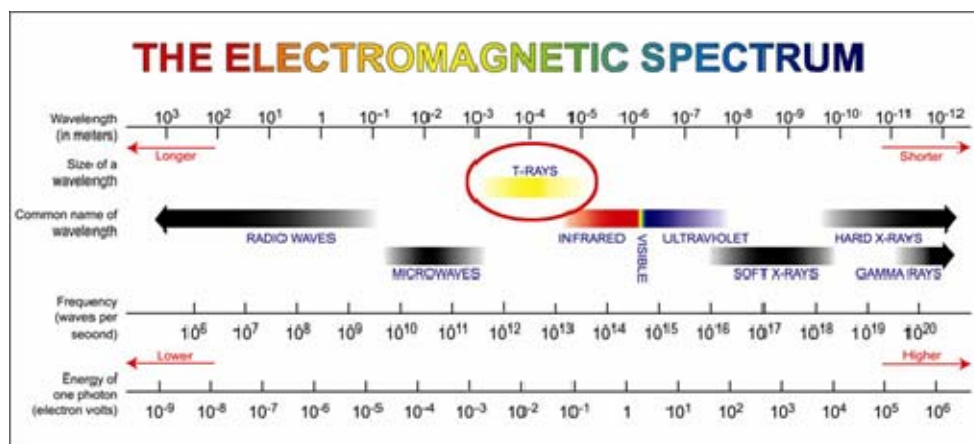


Fig. 1. Terahertz radiation (“T-rays”) with respect to rest of the electromagnetic spectrum (from [43]).

This void is not due to an absence of available applications in the terahertz regime. On the contrary, the relatively short wavelength and deep penetration properties of terahertz waves for most non-metals (as well as its strong reflective properties for metals) provide an outstanding opportunity for many types of high-resolution imaging. Some prominent potential applications of terahertz radiation are the visual screening of persons and packages for detection of concealed objects (firearms, knives, etc.), spectroscopic identification of explosive materials (such as IEDs in combat zones), and medical imaging of human tissue (e.g., for cancerous lesions). The additional fact that

terahertz radiation is entirely non-ionizing* and therefore relatively safe for human exposure further argues in favor of the utility of this frequency regime [9]-[11].

Technological exploitation of a particular frequency band, however, requires the development of both sources and detectors that operate there. In the case of terahertz radiation, there is a pronounced dearth of both. This deficiency is owing to the relatively small photon energies associated with terahertz waves, a characteristic that tends to render conventional methods of generation and detection infeasible in this regime. Ironically, while terahertz radiation quanta are not sufficiently energetic to be produced or detected using these so-called “optical” devices, they are, at the same time, *excessively* energetic for so-called “electronic” devices that easily produce millimeter-scale and microwave radiation [44].

Historically, it has been the sensor, rather than the source, that represents the greater engineering difficulty in the terahertz regime [42]. Methods which are used with great success for detection in the infrared regime (8-12 μm) are not necessarily compatible with the longer wavelengths associated with terahertz radiation. By far, the most common principle used in infrared imaging is that of photon detection by the process of electron-hole generation/recombination [42, [45]. In this method, photons which are passively emitted as graybody radiation from thermal sources are individually absorbed by bulk semiconductor materials; they directly produce electrons and/or holes that can be measured electronically to determine the incident photon flux. These detection systems can not, however, be operated satisfactorily at room temperature. The energy gap that is required for detection in this infrared regime is approximately 120 meV (for $\lambda \approx 10\mu\text{m}$). Although the value of kT for an object at room temperature is only 26 meV, there is high risk of the conduction band being populated by thermal excitation. (The intrinsic carrier concentration for semiconductor materials is typically about 10^{18}

* This property derives from the fact that THz photons do not contain sufficient energy per quanta to remove (i.e., ionize) an electron from an atom or molecule, and therefore cannot inflict significant damage to human DNA. In spite of this fact, thermal effects can arise in the skin from under extended THz exposure, and some studies have linked development of cataracts in the human eye under prolonged exposure to non-ionizing radiation. Nevertheless, the health hazards posed by THz radiation are significantly less than those posed by many conventional (e. g., x-ray) imaging technologies.

cm^{-3} at 300 K, which generates prohibitively large dark current in the detector.) Therefore, such detectors can perform satisfactorily only when operated at or below liquid nitrogen temperatures (77 K).

Furthermore, if this same technology is used to engineer a detection device with energy gap customized to the terahertz regime, thermal effects become completely intractable under all but the lowest cryogenic temperatures. Employing a photon detection approach at 1.0 THz, for instance, would require an energy gap of only 4 meV. Inasmuch as this energy value is nearly an order of magnitude lower than kT at room temperature, it is plain that operation of such a device in the terahertz regime can only be possible by cooling the device to cryogenic temperatures (preferably 4 K or less, for which $kT = 0.35$ meV). This is not to suggest that photon detection techniques are not an effective or viable terahertz imaging methodology. Indeed, such cryogenic operation has been used quite successfully for terahertz imaging. However, this success comes by incurring costs in convenience, compactness, and economics.

By introducing an entirely different type of technology, an effective sensing system can be designed for terahertz frequencies. Microbolometer arrays—comprised of micro-scale pixels with thermally-sensitive resistivities—have proven to be an effective basis for real-time infrared imaging systems; more recently, researchers at the Naval Postgraduate School (NPS) and the Massachusetts Institute of Technology (MIT) have independently shown that they are also at least modestly responsive to radiation oscillating at terahertz frequencies [34]-[41]. The goal of this dissertation research was to further investigate methods of terahertz detection using microbolometer technology with quantum cascade laser (QCL) sources, to establish techniques for characterizing and improving QCL output beam power, and—most importantly—to develop an optical scheme under which various objects (particularly metallic objects) can be imaged under THz illumination.

THIS PAGE INTENTIONALLY LEFT BLANK

III. THE SOURCE: QUANTUM CASCADE LASER (QCL)

A. QCL THEORY/BACKGROUND

As mentioned above, current scientific investigations of terahertz radiation suffer from a lack of available sources. However, as shown in Fig. 2, there are still roughly a half-dozen methodologies that are capable of producing either narrowband or broadband terahertz radiation. While these methods are typically bulky in both size and weight and not particularly amenable to the types of applications listed above, they currently provide the best opportunity for terahertz imaging trials available.

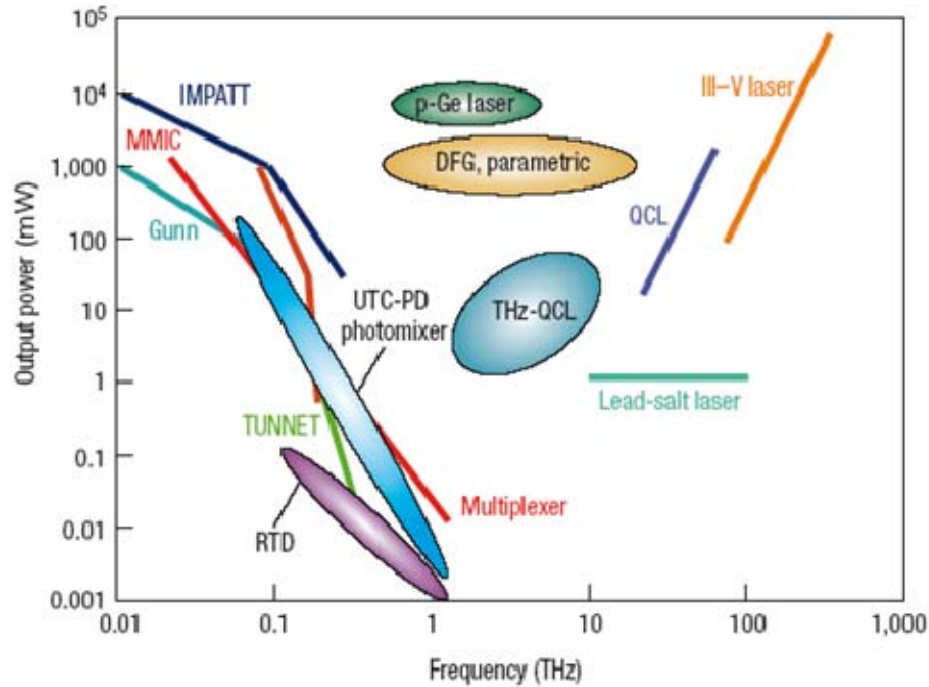


Fig. 2. Methods of producing terahertz radiation. “DFG” refers to difference-frequency generation, a technique which is used to generate the THz beam studied by the author during a late collaboration effort with Stanford University researchers. (from [46])

For the research reported in this dissertation, a pair of two quantum cascade lasers (QCLs) tuned to individually lase at 2.8 and 3.6 THz were used for nearly all imaging

experiments.[†] The lasers were fabricated by Professor Jérôme Faist's research group at the University of Neuchâtel in Switzerland and graciously provided, gratis, to the NPS Physics Department by Danielle Chamberlin and Peter Robrish of Agilent Laboratories in Santa Clara, CA.

The quantum cascade laser (QCL) is a special class of semiconductor laser that operates upon a fundamentally different design principle than the diode lasers that are frequently used for visible and near-infrared light generation [47]-[48]. While both types of lasers use electronic transitions between energy bands as the basis for photon generation, the manner and physical phenomenon by which this effect is produced is distinctly different. Diode lasers—the traditional, more common class of semiconductor laser—produce laser radiation via electronic transitions between conduction and valence bands. Owing to the principle of lowest energy, electron population of the lower-energy valence band is much greater than that of the conduction band; lasing is achieved in such devices by stimulating emission of a photon by forcing the recombination of an electron in the conduction band with a hole in the valence band. Because the energy of the band gap is uniquely fixed by selection of a particular bulk semiconductor material, each emitted photon has an energy equal to E_g . By electrically or optically pumping the semiconductor device, the normally miniscule electron and hole populations can be dramatically increased beyond the intrinsic carrier concentrations—allowing the sustainment of a population inversion, amplification by stimulated emission, and the output of a laser beam from the diode. Output power from the diode laser is given by the following equation [49]:

$$P = \frac{\eta h \nu (I - I_{th})}{2e}, \quad (1)$$

where h is Plank's constant, I and I_{th} are the applied and threshold current (respectively), e is the electrical charge of an electron, ν is the lasing frequency, and η is the total quantum efficiency of the device.

[†] A difference-frequency generated terahertz beam was also used in the very final stages of this research effort; however, these imaging trials involved only the beam (rather than individual objects) and were primarily used only to establish the detection threshold of the detector system.

In contrast, as first proposed by Kazarinov and Suris in 1971 [47] and experimentally demonstrated by Faist et al in 1994 [48], quantum cascade lasers are inherently unipolar devices. In QCLs, laser action is achieved exclusively through electron transitions between subbands within the conduction band. This subband structure is generated by fabricating the device with periodic, alternating layers of materials with different bandgaps (e.g., AlGaAs and GaAs) and varying thickness. The superlattice that is formed by this arrangement produces a one-dimensional quantum well confinement effect; it is this confinement that is responsible for splitting the energies associated with the conduction band into discrete electronic subbands in which electrons can reside [50]. Fig. 3 illustrates the energy level structure of a typical QCL designed to operate in mid-infrared wavelengths. This energy level diagram is sloped due to the application of an external electrical bias, which, as will be seen, drives the passage of electrons through the device from one active region to another.

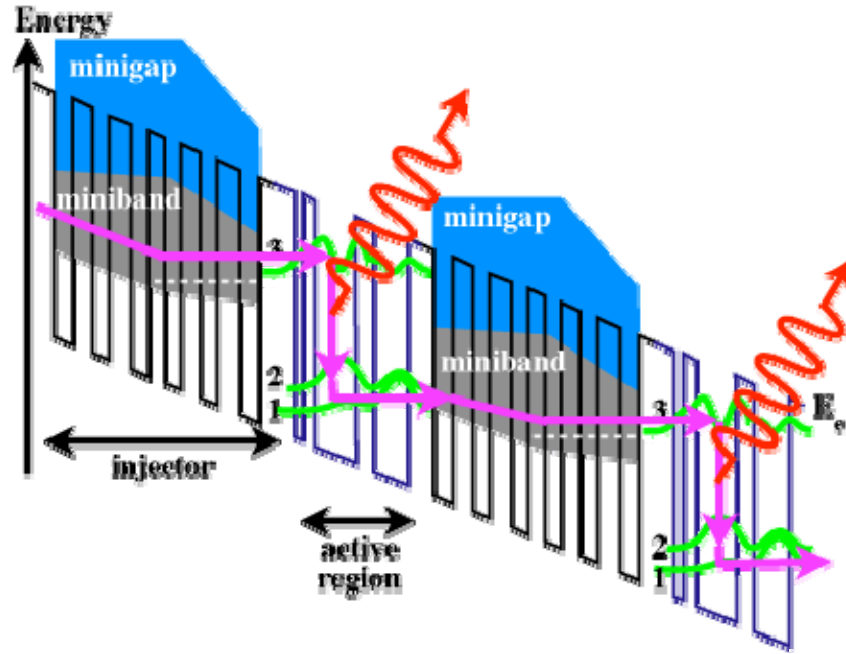


Fig. 3. Band structure of a conventional three-level QCL, in which depopulation from the discrete lower laser level is via optical-phonon interactions (from [52]).

The three-level structure of the conduction band is key to the laser's operation. Electrons injected into the upper subband (level 3) are dropped to level 2 within the active region by stimulated and spontaneous emission; each emits a photon in the process. To maintain population inversion between levels 3 and 2, rapid depopulation of level 2 is necessary. In the case of most QCLs, this is achieved by designing the energy difference between levels 1 and 2 to be resonant with the optical phonon energy of the laser material (typically GaAs). In this manner, resonant optical-phonon scattering ensures rapid (sub-picosecond) relaxation of electrons from level 2 to level 1 and therefore allows sustainment of a continual population inversion between levels 2 and 3 at lower applied currents (i.e., reduced threshold current).

The principal advantage of QCLs over other semiconductor lasers derives from the periodic design of the device and the unipolar nature of its operation. Because each transition is achieved without the involvement of holes, electrons are not annihilated after depopulating the upper laser level. This important distinction allows each electron to emit a single photon when transitioning from level 3 to level 2, to then rapidly transition from level 2 to level 1 through phonon scattering, and then tunnel from one active region of the quantum well structure (through the so-called injector region, identified in Fig. 3) and into an adjacent active region. Upon tunneling, each electron can then repeat the process again and again in a repetitious, cascading fashion (the process from which the QCL derives its name). Indeed, for a QCL fabricated with 120 periods, each electron can produce 120 resonant photons, thus significantly amplifying the total beam power that is eventually emitted from the device.

Thus it is seen that equation 1 presented above for conventional diode lasers is, also, quite applicable to QCLs—save for one important distinction. The two equations differ only by a factor of N , the number of periods in the laser, due to the multiplicative effect produced by the device's cascading structure [49]:

$$P = \frac{N \eta h \nu (I - I_{th})}{2e} \quad (2)$$

This multiplicative effect is especially important when dealing with terahertz lasers. Because the wavelengths associated with terahertz radiation are roughly an order of magnitude longer than those of infrared radiation, each terahertz photon carries only one-tenth the energy of one found in the infrared regime. (This difference is even more pronounced between terahertz and visible photon energies, which differ by a factor of roughly 500.) Moreover, the quantum efficiency factor, η , is found to take on lower values at longer wavelengths due to an attendant increase in optical losses within the cavity. On the other hand, because materials used in QCLs tend to have wider energy gaps than the narrow-gap bulk crystals used in other semiconductor devices, QCLs are capable of carrying much larger current densities than conventional diode lasers without incurring damage.[‡] As a result of both of these factors, QCL lasers can produce roughly one thousand times the output power of diode lasers operating at the same wavelength [49]. These advantages obviate any liabilities associated with the long wavelengths of the terahertz regime, and make QCLs a natural and effective choice of source for such radiation.

The above scheme provides an elegant and relatively efficient means of producing visible and infrared radiation alike. However, because terahertz photon energy is less than the optical phonon energies associated with the device’s semiconductor material (~ 32 meV for GaAs), it is not suitable for use in terahertz-tuned QCLs. Such an energy arrangement would require that the gap between the first and second energy levels be less than the gap between the second and the third levels—in violation of quantum confinement theory and the familiar “particle in a box” problem. As a result, QCLs designed for this regime (such as the one employed in the present study) employ a so-called “bound-to-continuum” transition design, in which the electrons undergo transitions from a bound state into a conduction miniband, rather than to a discrete energy state as in the QCL described above (Fig. 4).

[‡] This important advantage over diode lasers should not be interpreted as an assertion that QCLs can tolerate arbitrarily large bias currents without damage. During the course of this research, the 2.8 and 3.6 THz QCLs were each operated with an applied bias of roughly 500 A/cm². However, owing to the small dimensions of the laser’s alloyed contact pad (200 μ m \times 2 mm), this current density was delivered using a bias of only 2.0 A. It is expected that employing currents much higher than this value will result in destruction of the device—principally through irreversible Joule heating effects.

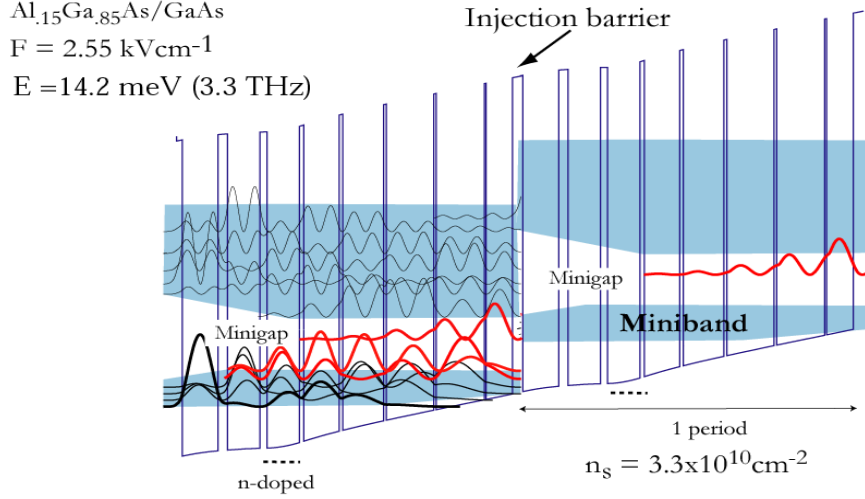


Fig. 4. Band structure of a bound-to-continuum quantum cascade laser, characteristic of the device used to produce terahertz radiation in the present research (from [53]).

An important distinguishing feature of the bound-to-continuum design involves the unique nature of this downward transition. Firstly, the transition is diagonal in the sense that the electron must tunnel across the injection region in order to drop to the miniband constituting the laser's ground state [50]. Secondly, depopulation of the ground state is achieved via electron thermalization rather than optical-phonon interaction. Upon dropping to the ground miniband and emitting terahertz photons in the process, electrons are rapidly removed by the external electric field, injected to the next adjacent bound state, and allowed to repeat the process for each of the laser's stages. In the 3.6 THz laser of this study [51], the basic QCL structure was produced by molecular beam epitaxy (MBE) as a set of alternating $\text{Al}_{0.15}\text{Ga}_{0.85}\text{As}$ and (GaAs) layers of width 12.1 (3.2), 11 (2.4), 11 (1.5), 12 (1.2), 13.8 (1.0), 16 (0.9), 16.3 (0.6), and 9 (4.5) nm. These alternating layers serve to produce two distinct regions within each structure: an active region (in which lasing occurs) and an injection region (through which electrons are resonantly tunneled from one active region to another). 120 periods of this structure, embedded in a single Plasmon waveguide with a confinement factor of $\Gamma=0.33$ and a waveguide loss of $\alpha_w = 4.6 \text{ cm}^{-1}$, produce a series of active regions with three conduction subbands that constitute the laser device.

B. TERAHERTZ QCL OPERATION

Injection of electrons into the active region is essential to the QCL's operation. Fig. 5, which illustrates the overall engineering and design of the 3.6 THz QCL device, provides insight into how this is accomplished. The repeating AlGaAs/GaAs quantum well structure ("MQW") described above and illustrated in Fig. 3 is grown upon a 250 μm thick substrate of semi-insulating GaAs and a 300 nm thick layer of n-doped GaAs [51]. The active region is approximately 14 μm thick; the ridge waveguide, processed by wet etching and three metallization steps, has dimensions of 2 mm by 200 μm . Current is applied to the alloyed contact layer above the MQW region. Because the non-radiative lifetime of electrons in level 3 of the active region is extremely short (roughly 1 ps), threshold current density for the device is relatively high. However, a consequence of the waveguide's relatively small dimensions is that arbitrarily high currents cannot be used without incurring significant Joule heating effects within the QCL device.

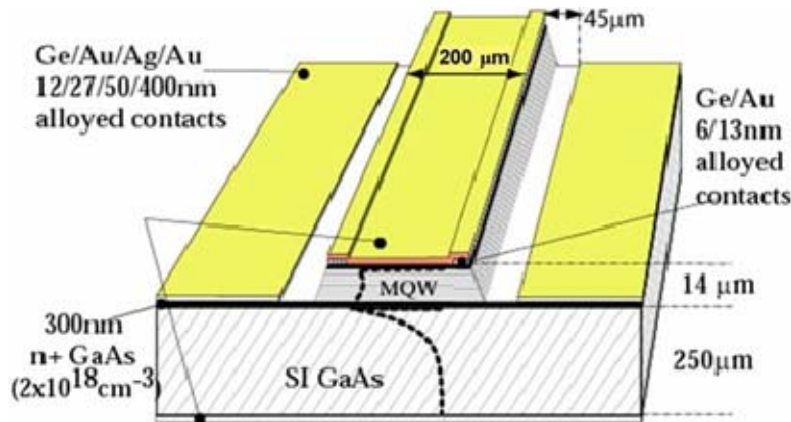


Fig. 5. Schematic of quantum cascade laser used in imaging experiments. The active region of the laser consists of 120 periods of GaAs/AlGaAs quantum wells (after [53]).

As a result, electrical pumping of the QCL must be approached with care. Application of a continuous current results in rapid heating of the laser and attendant thermal population of the upper laser level within the conduction subband. This effect, which is particularly deleterious in lasers operating at terahertz frequencies (due to the

exceptionally small energy level separations involved), fundamentally interferes with the process of stimulated photon emission; the end result is a significant reduction (if not extinction) of QCL output power.

To minimize thermal effects, such lasers are typically cooled to cryogenic temperatures (50 K or better) and operated in pulsed mode [51]. For the 3.6 THz laser predominantly used in the present study, a 300 kHz pulse repetition frequency (PRF) was typically used with 15-20% duty cycle (500-667 ns pulse width).[§] It is especially important in such cases to maximize the efficiency of electrical power transfer by eliminating any impedance mismatch that exists between the pulse generation apparatus and the QCL. Impedance of the pulse generator and associated cables are known; QCL impedance, however, can only be accurately obtained by recording its I-V characteristics during operation.

Matching was performed by evaluating the QCL's dynamic impedance and using the data to produce a step-down transformer with an appropriate number of windings for use in the electrical circuit [37]. Current-voltage (I-V) characteristics of the laser were measured by applying electrical pulses at a PRF of 300 kHz, and 5-25% duty cycle, over a range of applied voltages. For each increment of applied voltage, the current flowing through the laser was measured with a Pearson current monitor.

Analysis of current-voltage (I-V) data indicates that dynamic impedance of the QCL during operation is approximately 2.7Ω ; as seen in Fig. 6, this result is largely independent of duty cycle. Conversely, insofar as a larger applied voltage is required to produce a given current through the device at higher duty cycles, it is evident that static impedance increases for longer pulse widths. The reasons for this phenomenon have not yet been fully identified; however, it is possible to eliminate the possibility that it is strictly a temperature-driven effect arising from Joule heating. On the contrary, Fig. 7 (I-V data for various cryostat temperatures) clearly demonstrates that static impedance actually *decreases* with increasing cryostat temperature for the particular QCL under

[§] It should be noted that, although optimum results were obtained using the operating parameters mentioned, laser action was still achievable at duty cycles as low as 5% and as high as 25% (the results of which will be elucidated upon in the analysis section of this dissertation).

investigation. This is possibly a consequence of the fact that displacement current through the coaxial cable capacitors increases as the duty cycle becomes smaller.

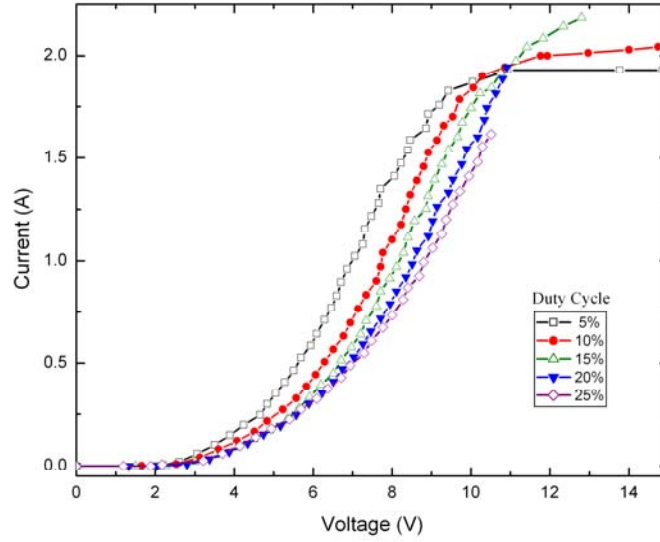


Fig. 6. I-V data for the 3.6-THz QCL, operated under various duty cycles. Dynamic impedance of the device is given by the reciprocal of the slope of the linear region of the curves.

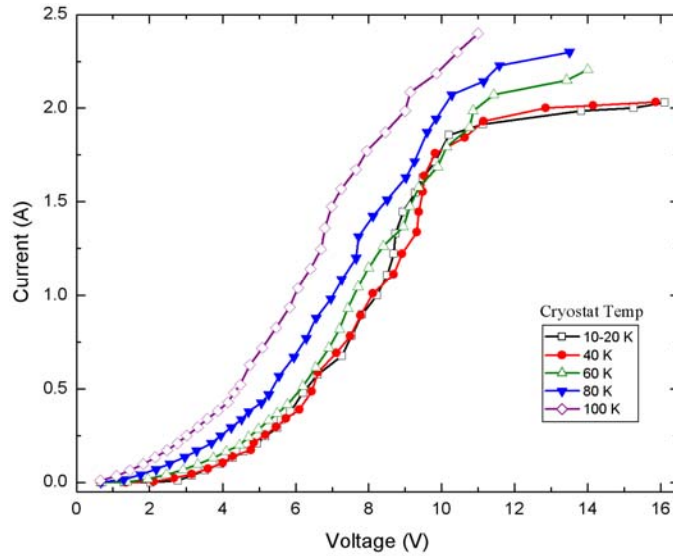


Fig. 7. I-V data of the 3.6-THz QCL, operated under 10% duty cycle, at various cryostat temperatures. The I-V data set labeled as “10-20 K” was collected with cold head thermostat set to 10 K; however, closed-cycle refrigeration was not sufficiently robust to prevent an elevation of temperature (by Joule heating), to as high as 20 K, at higher bias currents.

THIS PAGE INTENTIONALLY LEFT BLANK

IV. THE SENSOR: MICROBOLOMETER FPA

A. MICROBOLOMETER THEORY/ BACKGROUND

Because they operate upon a fundamentally different set of physical principles, thermal detectors such as microbolometers enjoy a significant advantage over conventional infrared photon detectors with respect to the detection of infrared radiation. Whereas photon detectors detect radiation through the creation of electron/hole pairs resulting from absorbed photons (and, thus, require cooling to cryogenic temperatures to prevent thermal excitation across the band gap), detection in bolometers is driven solely by temperature changes arising from absorption of photons by the pixel membrane layer [42]. Under normal operation in the infrared regime, graybody radiation—originating from objects within the camera’s field of view—falls upon the FPA; the distinct thermal response resulting in each pixel allows for the generation of images which are essentially graybody intensity maps of the scene before the camera. Since the core temperature of humans is typically ~ 10 K above that of room temperature (300K) and the NETD of most microbolometers is less than 0.1 K in the infrared regime [54], microbolometers can easily produce high-resolution images that clearly distinguish persons from their background environs and, indeed, from their clothing as well. Furthermore, this NETD value is sufficiently sensitive that high contrast is achievable in distinguishing fine features of the human body (e.g., the face) based upon differences in blood flow—and attendant temperature variations—to different regions (Fig. 8).



Fig. 8. Infrared image of the author, taken under conventional operation of the microbolometer camera used in this study (without optical modifications).

Because pixel response is determined by *differences* in temperature, ΔT , of the pixel relative to its ambient operating temperature, the system operates effectively at room temperature and does not require the types of cooling infrastructure incurred by conventional infrared imaging systems. Indeed, it is this room-temperature operation that allows microbolometer cameras to achieve their characteristic properties of compactness, low weight, and ruggedness (Fig. 9).



Fig. 9. The imaging system used in the present research: Infrared Solutions IR-160 infrared microbolometer camera (from [54]).

The difference between conventional bolometers and microbolometers (such as the type in this dissertation research) is principally one of physical scale. The underlying thermal physics of the two system types are fundamentally identical; however, in order to produce high-quality image resolution in the infrared regime, pixel pitch of a bolometer camera must be kept small (on the order of 50 μm). This is not possible using conventional engineering techniques, but is certainly achievable in the microelectromechanical (MEMS) domain. The fine degree of detail achievable in microbolometers is evident in the microphotograph of a single microbolometer pixel shown in Fig. 10.

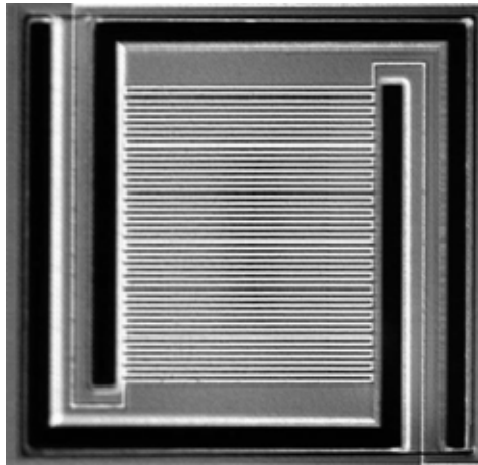


Fig. 10. The imaging system used in the present research: Infrared Solutions IR-160 infrared microbolometer camera (from [54]).

The architecture that supports the upper pixel layer shown in Fig. 10 is a relatively simple but elegant one (Fig. 11). By using MEMS process layering of silicon (Si), silicon nitride (Si_3N_4), vanadium oxide (VO_x), and sacrificial layers of silicon dioxide (SiO_2), a free-standing pixel membrane comprised of Si_3N_4 and VO_x can be produced that is thermally isolated from both the substrate layer (by virtue of support arms, which are also constructed of Si_3N_4) and adjacent pixels—thus eliminating the threat of any lateral heat flow which would severely degrade image quality. The active pixel element, often referred to as the “membrane layer,” is comprised of a layer of Si_3N_4

and applied VO_x film. The VO_x film, which exhibits a high temperature coefficient of resistance (TCR), is essential to device operation in the sense that it is the mechanism by which differences in incident radiation are detected as changes in pixel resistance. Each pixel is constructed such that a current bias can be applied (to allow for measuring of changes in voltage, ΔV , resulting from radiation/resistivity variations); support arms are designed so as to allow both electrical and thermal conduction to the substrate (which serves as a heat sink and electrical read-out mechanism). Typically, the FPA (and each pixel contained therein) is enclosed in an evacuated package, equipped with an IR-transmissive window, to eliminate any possible thermal conduction to the ambient atmosphere. Ideally, the only allowed pathway for thermal conduction from the pixel membrane should be through the support arms to the substrate [45]. Furthermore, if this exclusive conduction path is (through judicious design) minimized by designing the pixel with low overall thermal conductance, the principal heat loss mechanism becomes radiative in nature—allowing the array to operate at the background limit [45].

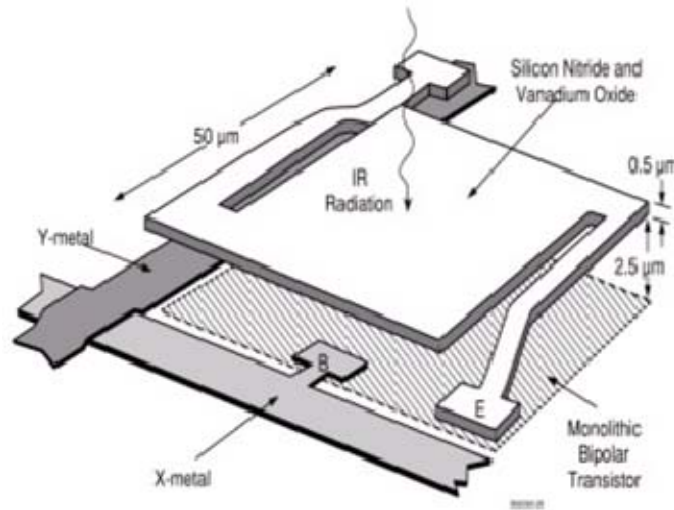


Fig. 11. Schematic of a typical MEMS-fabricated microbolometer pixel. Primary architectural elements (support arms and upper pixel membrane) are comprised of Si_3N_4 . VO_x is layered upon Si_3N_4 membrane to provide the pixel with a high TCR response to incident radiation. SiO_2 is used as a sacrificial layer to provide spatial separation of the membrane from the substrate layer, thus ensuring that the only thermal conduction allowed is that from the membrane through the support arms (from [55]).

Operation of a microbolometer detector is driven almost entirely by the physics of heat flow associated with each individual pixel. Specifically, the magnitude and rate of temperature change within the pixel determines the sensitivity and time constant of the camera [45]-[55]. To properly model these thermal characteristics, the standard heat flow equation is applied to obtain an analytic solution for pixel temperature change, ΔT .

Thermal energy incident upon the pixel in the form of external radiation (either in the form of passive or active illumination), P , may be dissipated through two primary mechanisms. Assuming convection and radiant heat losses are negligible, the thermal energy absorbed by the pixel partially manifests as a temperature increase in the pixel's sensitive region (directly proportional to the region's heat capacity, C , measured in J/K), and is partially dissipated by conductance to the support structure (proportional to the thermal conductance, G , measured in W/K). To the extent that the support structure (consisting of two micromachined arms) is attached to the constant-temperature substrate layer, this structure acts as a heat sink to the heated pixels [45].

Thus, heat flow into and out of the pixel can be represented with the first-order differential equation:

$$\eta P - C \frac{d(\Delta T)}{dt} - G(\Delta T) = 0 \quad (3)$$

where η represents the fraction of incident radiation that is actually absorbed by the pixel's sensitive layer. This fraction is largely dependent upon membrane emissivity, ϵ , and therefore can be significantly less than unity when the device is operated at wavelengths outside of the 8-14 μm design regime. Furthermore, assuming that the incident radiation is modulated at an angular frequency ω , in general the power term will contain an exponential factor, $\exp(j\omega t)$. Rearranging the equation in a form that allows solution by application of an integration factor, one obtains:

$$\frac{d(\Delta T)}{dt} + \frac{G}{C}(\Delta T) = \frac{\eta P_o}{C} e^{j\omega t} \quad (4)$$

The equation can be solved analytically by first using an integration factor, $u(t)$:

$$u(t) = e^{\int G/C dt} = \frac{C}{G} e^{Gt/C} \quad (5)$$

yielding the solution:

$$\Delta T(t) = \frac{\eta P_o}{C e^{Gt/C}} \int e^{(G/C + j\omega)t} dt = \frac{\eta P_o e^{-Gt/C}}{G + j\omega C} (e^{(G/C + j\omega)t} + K) = \frac{\eta P_o}{G + j\omega C} (e^{j\omega t} + K e^{-Gt/C}) \quad (6)$$

The integration constant, K, is obtained by applying any initial conditions known for ΔT . At $t=0$, the incident radiation has not yet warmed the pixel. Therefore, using $\Delta T(0)=0$:

$$\Delta T(0) = 0 = \frac{\eta P_o}{G + j\omega C} (1 + K) \quad (7)$$

yielding a value of $K=-1$. Assembled as a final time-dependent solution, then:

$$\Delta T(t) = \frac{\eta P_o}{G + j\omega C} (e^{j\omega t} - e^{-Gt/C}) \xrightarrow{t \rightarrow \infty} \frac{\eta P_o e^{j\omega t}}{G + j\omega C} \quad (8)$$

where the right-hand side of the equation reflects the fact that, with increasing time, the $\exp(-G t/C)$ term vanishes. Eventually, a quasi-steady state condition is achieved in which the pixel temperature sinusoidally increases and decreases with the same frequency at which the input power is modulated. When this condition is reached, the root-mean squared temperature difference, ΔT_{RMS} , is given by:

$$\Delta T_{RMS} = \sqrt{\left(\frac{\eta P_o e^{j\omega t}}{G + j\omega C} \right) \left(\frac{\eta P_o e^{-j\omega t}}{G - j\omega C} \right)} = \frac{\eta P_o}{\sqrt{G^2 + \omega^2 C^2}} = \frac{\eta P_o}{G \sqrt{1 + \omega^2 \tau^2}} \quad (9)$$

This final closed-form equation for ΔT_{RMS} makes use of the fact that the ratio C/G , having units of time, is in fact the thermal time constant of each pixel (and, by extension, of the aggregate detection system as well). For purposes of pixel response time, then, it is clear that small values of heat capacitance and large values of thermal conductance are desirable. This is a consequence of the fact that such a combination of parameters ensure quick dissipation of thermal energy from the pixel's sensitive region—ensuring that changes in the incident radiation are rapidly detected by the pixels. Indeed, it is this time constant which determines the camera frame rate; the two parameters are

inversely proportional to each other. A commonly-applied rule of thumb dictates that the pixel time constant be one-third the value of the reciprocal of the desired frame rate [45]. Therefore, in order to support a camera capable of imaging at TV-frame rates (30 Hz in the United States), individual pixel thermal constant must be no slower than 10 ms.

However, a fast time constant—while desirable—is not the only (nor, even, the most) important metric of microbolometer performance. As clearly indicated by equation 9, high thermal conductance adversely affects the critical figure of merit, ΔT (pixel temperature change). This is because high thermal conductance directly implies low thermal isolation. To the extent that it is through temperature changes produced by spatial and temporal differences in the incident radiation that the system operates, it is in fact generally more important that the pixels be designed such that thermal conductivity is as low as possible (while still allowing a relatively short time constant) [45]. This is equivalent to producing a pixel with excellent thermal isolation. By thermally isolating the pixel such that both conductive and convective transfer are minimized, *radiative* transfer becomes the principal mechanism by which thermal energy is transferred from the pixel.

To achieve radiation-limited operation, then, convective and conductive transfer to the atmosphere is minimized by evacuating the capsule in which the focal plane array is packaged. As a result, conductive transfer to the support structure becomes the predominant process of thermal dissipation from the pixel's sensitive region—and is minimized through careful selection of materials and dimensions used for the support structure. Indeed, due to the importance of thermal isolation to pixel performance, design of a microbolometer generally begins with the design of the support structure. Thermal conductance is a property that is analogous to electrical conductance (the reciprocal of electrical resistance) in that it is directly proportional to the cross-sectional area, but inversely proportional to the length, of a conductor. It follows that low thermal conductance can be obtained by fabricating support arms of a insulator-type material

(Si₃N₄ is a typical choice) with long length but small thickness and width. Only after securing a well-isolated pixel architecture are pixel responsivity and thermal response time considered.

With temperature characteristics of the pixel, $\Delta T(P_o)$, thus defined, it is a straightforward matter to develop an expression for the manner in which such temperature changes produce a pixel-specific output voltage to the FPA. As mentioned above, the pixel's sensitive region is a thin ($< 1 \mu\text{m}$) membrane jointly comprised of both an absorbing layer and a high-TCR layer. The latter layer (commonly made of vanadium oxide, VO_x) typically has a temperature coefficient of resistance of $-.023/\text{K}$ [55], although magnitudes as high as $-.045/\text{K}$ are attainable using alternate preparation methods [56].

By definition, TCR (often given the variable α) is equal to the differential change in resistance with temperature, expressed as a percentage [55]:

$$\alpha = \frac{1}{R} \frac{dR}{dT} \quad (10)$$

Integrating this equation provides an expression for the total change in pixel resistance for a given rise in temperature. As with most semiconductors, this value is negative—indicating, unlike metals or superconductors, that resistance decreases with increasing ΔT . By multiplying equation 10 by dT and integrating the left- and right-hand sides of the resulting formula with respect to T and R , respectively, one obtains:

$$\int_{R_o}^{R'} \frac{dR}{R} = \ln(R') - \ln(R_o) = \ln\left(\frac{R'}{R_o}\right) = \int_{T_o}^{T'} \alpha dT = \alpha(T' - T_o) \quad (11)$$

where the naught subscript and prime superscript denote the initial and final values, respectively, of either T or R . Taking the exponential of both sides and making use of the fact that temperature increases within the pixel membrane layer are sufficiently small that the truncated expansion $\exp(x) \approx 1+x$ can be used with accuracy, one obtains:

$$\frac{R'}{R_o} = e^{\alpha(T'-T_o)} \approx 1 + \alpha(T'-T_o) \quad (12)$$

yielding, finally, an expression (with $\Delta R = R' - R_o$ and $\Delta T = T' - T_o$) that is valid for relatively small values of ΔT (the regime in which ΔR changes linearly with ΔT):

$$\Delta R = \alpha R_o \Delta T \quad (13)$$

The output voltage from a single pixel is produced by an applied bias current, i_b , and the resistance change ΔR that is produced by ΔT in the pixel membrane. Combining Ohm's law with equation 9, this signal voltage takes the form:

$$V_s = i_b \Delta R = i_b \alpha R_o \Delta T = \frac{P_o i_b \alpha R \eta}{G \sqrt{1 + \omega^2 \tau^2}} \quad (14)$$

By dividing equation 14 by P_o , then, one obtains an expression for voltage responsivity, \mathfrak{R}_v —a critical metric for any detection system:

$$\mathfrak{R}_v = \frac{V_s}{P_o} = \frac{i_b \alpha R \eta}{G \sqrt{1 + \omega^2 \tau^2}} \quad (15)$$

Here, again, one sees the prime importance of a low-G value to detector performance. Thermal conductance of the pixel figures prominently into every important figure of merit that is associated with microbolometer sensitivity. Low thermal conduction is especially important as it relates to pixel “crosstalk.” If the pixels are not sufficiently spaced (or worse, are contiguous) within the focal plane array, the resulting lateral heat flow between pixels will result in a loss of image resolution. Indeed, it is for this reason that most microbolometer designs begin with a selection of dimensions and material for the support structure that produce the lowest G possible. After settling upon a specific microbolometer design—and evaluating the pixel thermal conductance that results from it—work begins on developing a membrane heat capacity which allows detector operation with a particular time constant (as determined by the relationship $\tau = C/G$). This heat capacity value is a function of thickness, specific heat, electrical contacts, detecting material, and coating of the pixel; as such, many engineering options are available for the purpose of securing a particular frame rates (typically 30 Hz) for the camera [45].

As suggested mathematically in equation 9, there are two sets of limiting cases that arise for ΔT_{RMS} —corresponding to high and low modulation frequencies. For

situations in which the angular modulation frequency is much faster than the camera frame rate ($\omega \gg 1/\tau$), ΔT is largely driven by the modulation frequency and heat capacity:

$$\Delta T_{RMS} \approx \frac{\eta P_o}{G \omega \tau} = \frac{\eta P_o}{\omega C} \quad (\omega \tau \gg 1) \quad (16)$$

For operating conditions in which the angular modulation frequency is much slower than the camera frame rate ($\omega \ll 1/\tau$), ΔT is principally limited by the thermal conductance of the support structure, G .

$$\Delta T_{RMS} \approx \frac{\eta P_o}{G} \quad (\omega \tau \ll 1) \quad (17)$$

As will be seen in the following sections of this dissertation, the QCL employed in this research is typically operated at a 300-kHz repetition rate. For a typical time constant of 10 ms, then, it is clear that the microbolometer effectively operates within the “high-frequency” regime described by equation (11). Thus, equation 17 serves to identify the order of temperature change that can be expected to occur within the pixel in response to a particular incident power density.

B. NOISE ANALYSIS

The metric most commonly used to quantify sensitivity of a thermal imaging system, noise equivalent temperature difference (NETD), is defined as the temperature change in a large blackbody, within the field of view of an imaging system, that causes the signal-to-noise ratio at circuit readout to change by unity [45]. NETD is sensitive to both the optical characteristics of the imaging system and, especially, the pixel noise equivalent power (NEP). It follows that a thorough examination of the system’s noise sources is a necessary prerequisite for properly evaluating camera sensitivity.

The microbolometer camera used in this research (IR-160, Infrared Solutions) utilizes a 160×120 pixel FPA which is sensitive to radiation falling within the 8-14 μm wavelength range. With over 35% of total radiative power of the 300 K blackbody spectrum lying within this range, the device has a relatively low noise equivalent temperature difference (NETD) at room temperature; this sensitivity allows for

generation of high-quality infrared images under passive operation (i.e., no external illumination is necessary). When operated in the infrared regime, the camera has a dynamic range of 66 dB and NETD of less than 100 mK with f/0.8 optics [54].

These radiometric conditions, which allow for outstanding performance in the infrared regime, act as technical obstacles to a microbolometer detector operating in the terahertz regime. As graphically depicted in Fig. 12, total radiative power emitted by a 300 K blackbody in the 1-5 THz spectral range is only one-twentieth of that associated with the design infrared band. Due to this stark disparity in available illumination power—coupled with the fact that IR-tuned microbolometer pixels exhibit sharply diminished absorption at terahertz frequencies—sensitivity of the FPA for the 1-5 THz band of interest was separately evaluated to establish whether external illumination is required to operate the device at such frequencies.

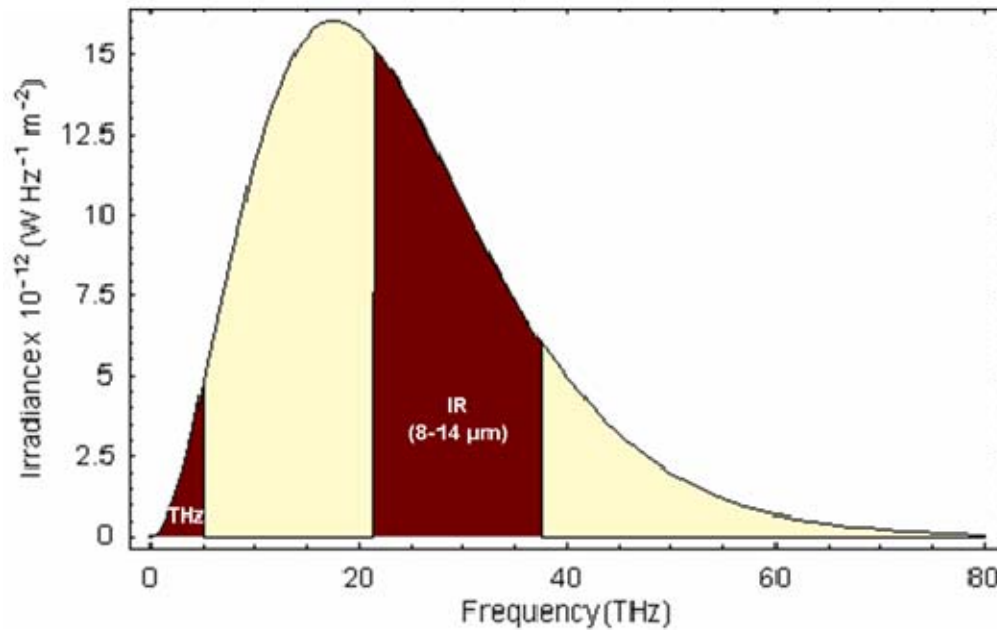


Fig. 12. Planck radiation curve for a 300 K (room temperature) blackbody, showing spectral irradiance as a function of frequency. The area of the left and right shaded regions represents total power density associated with the 1-5 THz and 21.4-37.5 THz (8-14 μm) spectral band, respectively.

As a function of noise equivalent power (NEP), NETD is given by [55]:

$$NETD = \frac{4 F_{no}^2}{A_{det} \varepsilon \pi T_l (dL/dT)} NEP \quad (18)$$

where F_{no} is the f-number of the optics used for focusing the beam onto the FPA, A_{det} is the area of a single pixel, ε is the emissivity of the membrane material, and T_l is the lens transmissivity. L , the spectral irradiance of the source, is given by [57]:

$$L(T) = \frac{\varepsilon_t P(T)}{\pi} \quad (19)$$

where ε_t is the emissivity of the illumination source and $P(T)$ is the exitance of the source in the terahertz frequency range of interest. Using Planck's radiation law and the fact that, at 300 K, $h\nu < kT$ for the 1-5 THz range [57]:

$$P(T) \approx \int_0^{\nu_c} \frac{2\pi k T}{c^2} \nu^2 d\nu \approx \frac{2\pi k T}{3c^2} \nu_c^3 \quad (20)$$

where ν_c is the high frequency cutoff of the terahertz region (5 THz). This formula yields a total incident power density over the 1-5 THz region of approximately 12 W/m² at 300 K—significantly less than that associated with the 8-14 μ m wavelength range (~ 170 W/m²). Thus, the NETD of the detector in the terahertz regime can be succinctly expressed as:

$$NETD = \frac{6 c^2 F_{no}^2}{A_{det} \varepsilon \pi T_l k \varepsilon_t \nu_c^3} NEP \quad (21)$$

The microbolometer camera used in the present study employs an f/1 lens with $A_{det} = 50 \times 50 \mu\text{m}^2$. Assuming a blackbody source, ε_t can be taken to be unity. Noise equivalent power is evaluated by first considering the various sources of noise within the detector. In microbolometers, the predominant noise source at lower readout bias currents is Johnson's [55]. At room temperature, the RMS voltage of this noise contribution is given by [57]:

$$V_{JN} = [4 k_B T R \Delta f]^{1/2} = 7.0 \mu V \quad (22)$$

where $R = 10 \text{ k}\Omega$ is the equivalent resistance for noise analysis when the microbolometer and $20\text{-k}\Omega$ load resistor are serially connected in the readout circuit [55]. The frequency bandwidth, $\Delta f = 0.29 \text{ MHz}$, is obtained from the 30 Hz frame rate at which the FPA's 160×120 pixel array is individually sampled. It follows that detector NEP, given by the ratio of V_{IN} to detector responsivity, $\mathcal{R}_v = 2 \times 10^5 \text{ V/W}$ [55], is approximately 35 pW .

As a result of optical modifications intended to maximize the amount of terahertz radiation received by the FPA, two of the optical parameters in Eqn. 4 (T_l , F_{no}) differ from those for the original system. Early experiments using the camera's stock germanium (Ge) lens indicated that the incident terahertz beam was strongly attenuated by anti-reflection coatings applied to the lens; to correct this deficiency, the Ge lens was replaced with a 1-inch diameter, 20-mm focal length bi-convex $f/1$ lens made of Tsurupica (PPL-1"-20mm-BC, Microtech Instruments). For focusing of the incident collimated beam, the lens was mounted 20 mm from the FPA, yielding an effective camera field of view of 53° . Tsurupica (formerly known by the trade name Picarin), measured to have a transmissivity (T_l) of 0.65 at 2.8 THz , was also used as the source material for the 2-inch diameter, 4-mm thick cryostat window. The emissivity metric ϵ , which is directly proportional to the membrane's absorption of incident radiation, has not been well characterized for terahertz frequencies. By using infrared emissivity values, however, one can obtain an upper-limit of detector performance and establish whether external illumination is necessary under the most liberal of assumptions. Using $\epsilon = 0.8$ (a well-documented value for the $8\text{-}12 \text{ }\mu\text{m}$ wavelength range [55]), the NETD of the microbolometer is found to be approximately 3 K . This result, which is more than an order of magnitude higher than the commercially-specified NETD of the camera for passive infrared imaging (0.1 K), confirms the need for external illumination when using the microbolometer camera at terahertz frequencies.

THIS PAGE INTENTIONALLY LEFT BLANK

V. EXPERIMENTAL PROCEDURES

A. IMAGING ARRANGEMENT

Having completed the theoretical and experimental foundations for development of a terahertz imaging system, next began the more vexing procedure of actually demonstrating that such an imaging technology is, in fact, achievable in practice. To this end, initial imaging trials were conducted in 2005 by Karunasiri, Chamberlin and Robrish at Agilent Laboratories with the 3.6-THz QCL and IR-160 microbolometer camera as source and sensor, respectively [34]. During these early feasibility trials, the QCL's optical configuration was as shown in Fig. 13. To accommodate the stringent cooling conditions required of the laser, the QCL was attached within a closed-cycle refrigeration chamber (maintained at 10 K temperature) using a copper-based laser mount to achieve good thermal conductance. Also mounted to the copper carrier were a one-inch diameter, 90-degree off-axis parabolic and an 80x80 mm² flat mirror for collimating and redirecting the laser beam through the cryostat window to the detection system. Both mirrors were gold-plated to allow maximum reflection of the QCL beam; copper was chosen for the mounting material to optimize heat transfer away from the laser during operation. The microbolometer was used in its original commercial configuration with the FPA sampled at a 30-Hz frame rate.

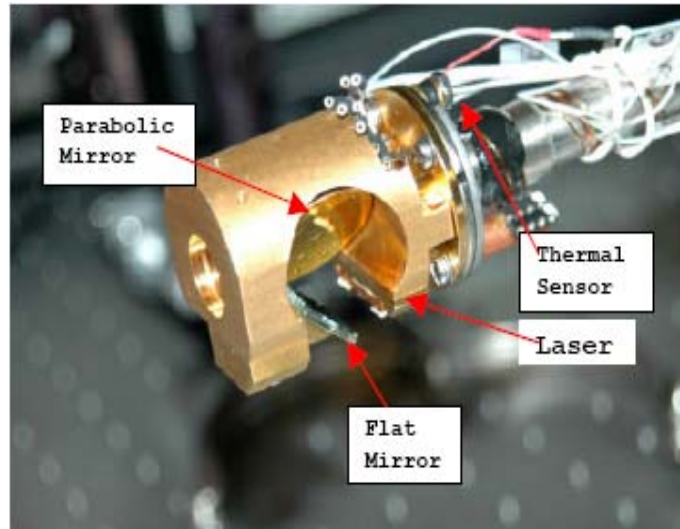


Fig. 13. QCL assembly used in initial imaging trials. QCL was mounted such that beam is emitted horizontally onto a flat mirror, then further reflected off of a parabolic mirror before exiting the chamber through a Tsurupica-based window (from [37]).

Initial imaging experiments conducted under this configuration failed to produce any signal whatsoever. Further examination suggested that this failure was likely due not to a lack of absorption by the pixel membrane layer, but, rather, the presence of antireflective (AR) coatings on the camera's original germanium-based lens element. Terahertz radiation is a full order of magnitude longer than the infrared radiation for which the microbolometer is designed; consequently, it followed that this AR coating was possibly acting as an absorbing medium to the QCL's output beam. This suspicion was confirmed when, upon removing the lens element entirely from the IR-160, the terahertz beam was immediately detectable by the FPA as a (roughly circular) bright patch [34]. Camera output was recorded at a 18 Hz frame rate using frame grabber software (Fig. 14).

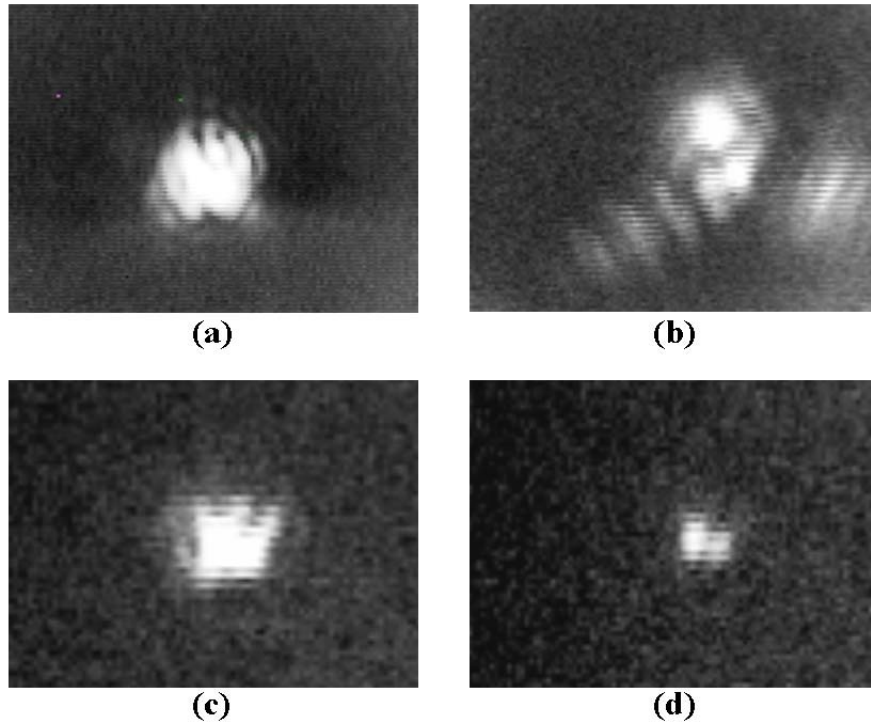


Fig. 14. Still images of video clips (taken by a frame grabber at 18 Hz frame rate) of real-time terahertz detection using a 3.6-THz QCL and IR-160 microbolometer FPA. (a) Unobstructed beam. (b) Beam with a metal pen passing between beam source and detector. (c) Beam obstructed by one sheet of bond paper. (d) Beam obstructed by two sheets of paper.

Fig. 14(a) is a video recording of the imaging results produced using the virgin beam only; Fig. 14(b) is video of the same beam, disturbed by a metal pen passing through the region between the QCL and detector. Fig. 14(c) and Fig. 14(d), video recordings of the QCL beam obstructed by common bond paper, serve to illustrate the detection capability of the system under more demanding imaging conditions. These latter two images established the important fact that the QCL beam is still detectable after passage through one or more layers of opaque nonmetallic materials, thus confirming that this optical scheme could indeed be leveraged for use in practical imaging applications.

Along with independent investigations conducted in the same year at the Massachusetts Institute of Technology (MIT) [35], these NPS-Agilent experiments were among the first to ever successfully demonstrate real-time, uncooled detection of terahertz radiation using a microbolometer FPA. Upon completion of initial studies,

Agilent researchers provided their 2.8 and 3.6 THz lasers, gratis, to the Naval Postgraduate School for purposes of continuing this research activity. At that time, Lowe, Karunasiri and the author began efforts to improve the detection results obtained using the same source/sensor system. Specifically, this entailed successfully evolving a system which merely *detects* terahertz radiation into one capable of high-resolution *imaging* of objects placed within the path of the beam. This clearly required the integration of a new lens element to replace the camera's Ge-based lens, which had been found to frustrate initial attempts at terahertz detection. To this end, NPS purchased two Tsurupica-based lenses (one f/1 bi-convex lens of $f = 20$ mm; one f/1.7 aspheric lens of $f = 50$ mm) from Microtech, Inc. that were specifically designed for use in optical systems employing terahertz radiation. Furthermore, an additional off-axis parabolic mirror was added to the optical path, external to the cold head, for steering and focusing the beam such that a collimated beam was presented to the region immediately in front of the camera. One of the two Tsurupica lenses was then placed one focal length away from the camera FPA to ensure a focused image on the focal plane. Finally, a Tsurupica-based window was installed in the cryostat to maximize transmission of the terahertz beam from the QCL through the cold head assembly. (Glass, which is known to partially attenuate terahertz radiation, was used for the original cryostat window.) Transmittance of Tsurupica in the terahertz regime was measured using Fourier Transform Infrared (FTIR) spectroscopy; as seen in Fig. 15, these measurements indicate that transmittance at 2.7 and 3.6 THz is approximately 65% and 61%, respectively.

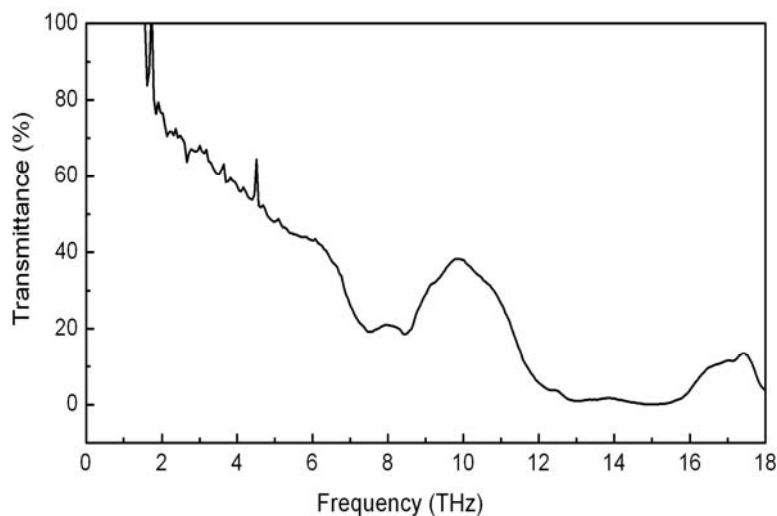


Fig. 15. Measured transmittance of a Tsurupica window as a function of frequency in the terahertz regime.

Imaging experiments were then attempted by placing various objects (metallic and nonmetallic) between the external parabolic mirror and the IR-160 camera. In spite of these optical improvements, operation of the source/sensor system with the two new lenses failed to produce any images that substantially improved upon the original results obtained at Agilent by Karunasiri, Chamberlin and Robrish. As before, metal objects strongly attenuated the beam through absorption; nonmetallic objects were, in the main, effectively penetrated by the beam. However, attempts to focus the physical profiles of metallic and nonmetallic objects alike were decidedly unsuccessful [37].

Beginning in early 2007, the author and Karunasiri implemented further engineering changes in the optical configuration of the terahertz detection system. Two principal deficiencies were identified as possible reasons for the inability to produce improved imaging results. Firstly, two of the system's four imaging elements (the one-inch diameter parabolic mirror and the $80 \times 80 \text{ mm}^2$ flat mirror) were internal to the cryostat and thus completely inaccessible (for adjustment) during imaging experiments. Secondly, the laser assembly was positioned approximately two inches from the cryostat window—a displacement which does not promote optimal transfer of laser energy from the cryostat.

To correct these engineering deficiencies, a new copper mount was designed and (with much-appreciated assistance from NPS/PH staff members George Jaksha and Sam Barone) fabricated. As shown in Fig. 16, the new mounting block was much larger in size (to further improve the rate of heat transfer away from QCL during lasing) and contained no optical elements whatsoever. The QCL was mounted within a slot on the left side of the copper mount using low-temperature conducting epoxy. When enclosed within the cold head, this left side of the mount was separated from the cryostat wall by less than 1.5 cm—thus allowing full passage of the QCL beam through the Tsurupica window.

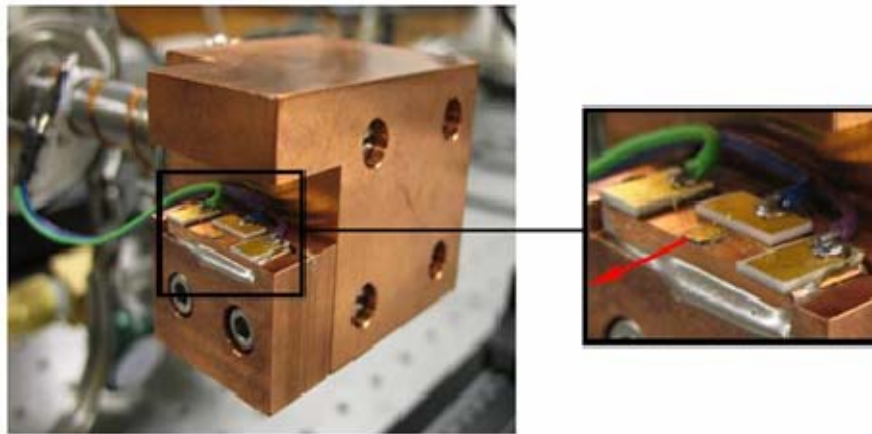


Fig. 16. Second QCL assembly design used within cryostat (with external cold head housing removed). Laser element is affixed to a copper carrier to facilitate transfer of thermal energy away from the laser. When lasing, beam is emitted outward, from QCL edge, along direction of red arrow (inset).

The final optical arrangement was as shown in Fig. 17. External to the cryostat were placed a pair of gold-plated, 90-degree off-axis parabolic reflectors ($f/1$ and $f/2$, each 50.8 mm in diameter) for focusing and steering the beam toward the camera. To minimize lateral alignment error, these reflectors were mounted upon a single optical post, and were positioned such that the highly divergent beam exiting the cold head was focused to a collimated state upon reaching the microbolometer camera. To achieve this state, the $f/2$ OAP was displaced 25 mm from the $f/1$ OAP, which was positioned 32 mm from the cryostat window. The 20-mm focal length ($f/1$) Tsurupica lens was mounted to

the camera within a custom-designed lens assembly that replaced the original (discarded) germanium lens package mentioned previously. To properly focus the incident (collimated) beam, the lens was mounted one focal length (20 mm) from the FPA, yielding an effective camera field of view of 53°. Ideal illumination of the FPA was found to result for a camera position (as measured with respect to the centroid of the Tsurupica lens) with 90 mm displacement from the $f/2$ OAP. Imaging experiments were then performed by inserting various objects roughly midway between the two parabolic mirrors, which produced a focused image at the microbolometer FPA. As suggested by the spatially close integration of components in Fig. 17, the total optical path length of this new configuration was kept as short as possible (within focusing constraints) to minimize beam absorption by the ambient air.

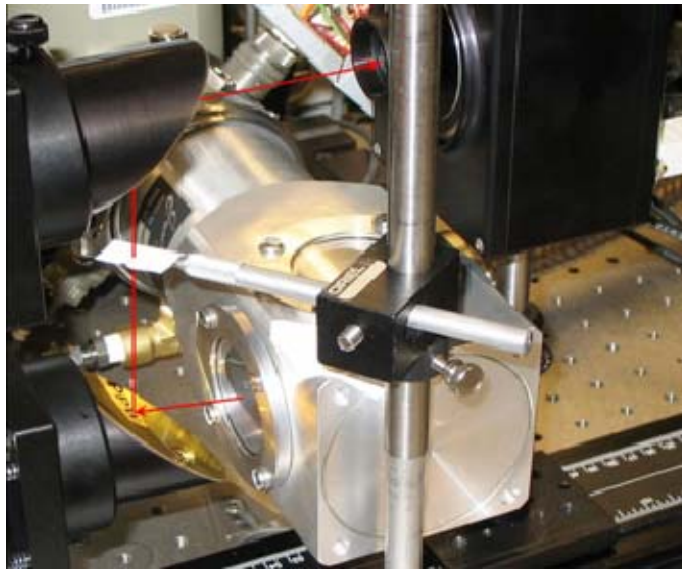


Fig. 17. Optical configuration used in most recent series of terahertz imaging experiments. Lower and upper mirrors (50.8 mm and 101.6 mm focal length, respectively) were used to focus and steer the terahertz beam emerging from the Tsurupica window of the cryostat to the focal plane array of the microbolometer (beam path is illustrated by red arrow).

This new optical configuration immediately yielded a dramatic improvement in imaging results. These images, which are presented in detail in the following chapter, provided exceptionally high resolution of metal and non-metal materials alike under illumination by both the 2.7- and 3.6-THz QCL beams.

B. FTIR ANALYSIS

Fourier transform infrared (FTIR) spectroscopy analysis (performed at a resolution of 1 cm^{-1} and a mirror speed of 0.64 m/s) provided important information about the spectral nature of the QCL beam. Perhaps most notably, it revealed that the “3.4-THz” QCL provided by Agilent was, in fact, a 3.6-THz laser.^{**} Apart from this minor but important technical revelation, FTIR spectroscopy established the spectral lineshape associated with a typical QCL beam. As seen in Fig. 18, the full-width, half-maximum (FWHM) spectral width of the QCL beam is approximately 45 GHz, with resonance occurring at 3.57 THz (with both values exhibiting slight sensitivity to applied duty cycle). As expected, QCL output power was found to generally increase with increasing duty cycle. FTIR analysis also provided an opportunity to further understand the relationship between duty cycle and output power over a range of applied bias currents.

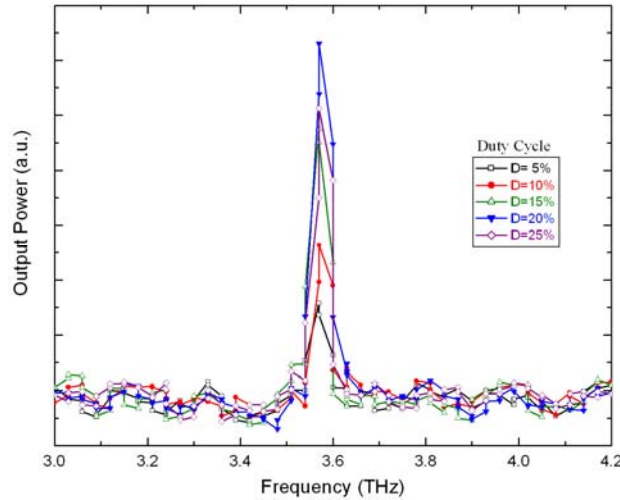


Fig. 18. Optical configuration used to conduct FTIR measurements of 3.6-THz QCL beam. A gold-coated, $f/1$ parabolic reflector was used with a silver-coated parabolic reflector for focusing and directing the beam into the external port of the FTIR spectrometer. Measurements were taken with the QCL operating under an applied bias of 1.6-1.7 A.

^{**} It is perhaps worth clarifying, at this point, that this disparity (3.4-THz vs. 3.6-THz) is the reason that two conference presentations by the author in early 2007 contain “3.4-THz” in the title. These presentations were prepared under the assumption that, per manufacturer’s claims, 3.4-THz was indeed the lasing frequency of the QCL. Not until after the conclusion of the two conferences was the above-mentioned FTIR analysis performed, yielding the 3.6-THz value which is now known to be the actual resonance frequency.

Fig. 19 shows measured output power of the laser for applied bias of 1.0-2.2 A, as measured by FTIR spectroscopy. The laser was operated at duty cycles of 5-25% (170-830 ns pulse length) to determine optimal pulse conditions for use in imaging experiments. Signal strength was measured by feeding the QCL beam through the external port of the spectrometer and measuring the height of the resulting peak. Higher duty cycles were found to generally produce higher output power; however, as further investigations confirmed, such conditions tend to rapidly warm the laser assembly via Joule heating effects. Each FTIR measurement (consisting of 16 scans) was taken over approximately 35 seconds with an initial cryostat temperature of 10K; therefore, the results presented in Fig. 19 are only representative of the *initial* output power from the laser.

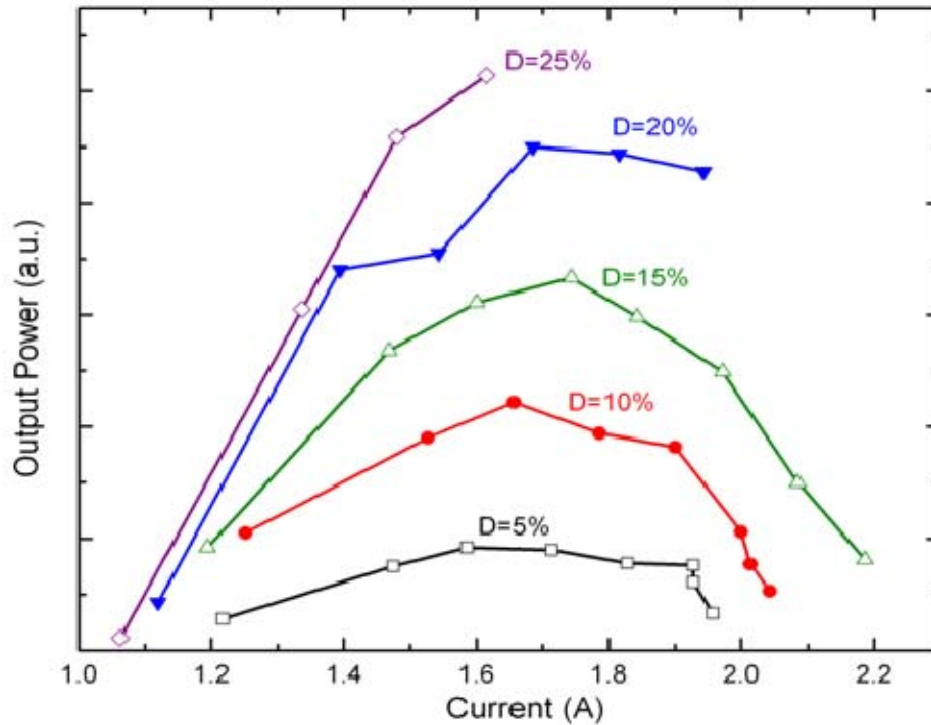


Fig. 19. Output power as a function of current for various duty cycles (D). Each data point was collected by FTIR spectroscopy using 16 scans at a resolution of 1 cm^{-1} and a mirror speed of 0.64 m/s .

C. FPA SENSITIVITY

Another, equally important method of QCL beam characterization involves assessing FPA sensitivity to the incident beam. To the extent that the microbolometer cannot produce images with a beam that is poorly absorbed by the FPA, this evaluation was essential to optimizing the image quality obtainable by the source/sensor system. This was done by measuring FPA signal intensity, for a specific duty cycle, as a function of the laser bias current. Fig. 20 reports the measured signal intensity of the laser while operating at a 15% duty cycle, overlaid with a corresponding V-I curve. Signal intensity of each microbolometer image was calculated by using a computer algorithm to deconstruct the image, evaluate the brightness of each of the 19,200 pixels, and sum the result. For these particular operating conditions, threshold lasing was achieved at approximately 1.0 A; lasing was found to cease beyond 2.2 A primarily due to (1) misalignment of energy levels due to large bias in the device and (2) excessive heating of the active region, originating from this same bias current, and resulting in thermal population of the middle laser level. Maximum beam intensity was achieved at 1.8 A with a bias voltage of about 10.5 V. For illustrative purposes, representative images of FPA output are included as inset frames within Fig. 20. The dual nature of this figure (reporting both voltage and intensity vs. bias current) is useful in that it illustrates a recurring trend that is observable for this and other duty cycles. Specifically, measured intensity tends to rapidly decline for bias currents above that value at which the QCL V-I curve ceases to be linear (approximately 1.9 A).

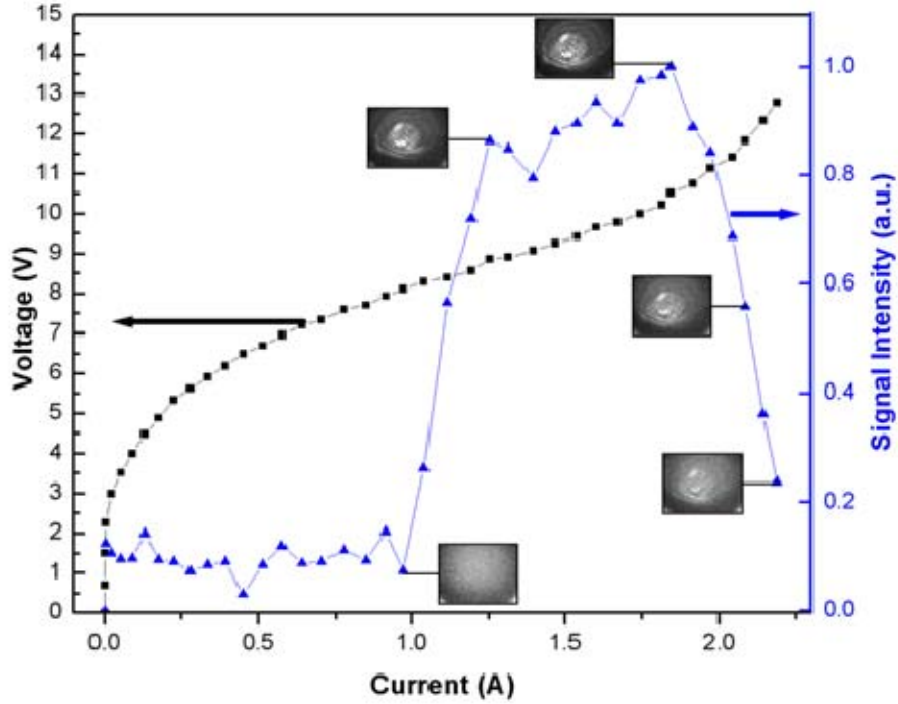


Fig. 20. Measured voltage across the laser and normalized image intensity of the QCL, operated at 15% duty cycle, as a function of current. The image quality associated with specific levels of signal intensity is illustrated by the inset images, taken by microbolometer FPA, of an unobstructed beam at operating currents of 1.0 A, 1.3 A, 1.8 A, 2.1 A, and 2.2 A.

D. IMPACT OF QCL TEMPERATURE ON IMAGING RESULTS

As alluded to above, the preceding graphs representing output power and signal intensity must be viewed with the caveat that they are, in the main, only indicative of beam strength over relatively short periods of time. Especially at higher bias currents and/or higher duty cycles, they reflect values obtained before Joule heating effects accumulate to the point of adversely affecting QCL performance. These effects are certainly not negligible; rather, they figure prominently into the system's practical viability as an imaging apparatus. Fig. 21 serves to illustrate cryostat temperature, at various duty cycles, over prolonged periods of time. Notwithstanding the fact that the cryostat was set to 10 K in each case, close-cycle refrigeration is not sufficiently robust to completely overcome Joule heating of the laser during operation. As a result, temperature of the laser assembly rises until reaching a steady-state value that is

dependent upon the applied voltage bias and selected duty cycle. (For the conditions under which Fig. 21 data were collected, these temperatures were 18, 21, 24, and 32 K for duty cycles of 10%, 15%, 20%, and 25%, respectively). The only case in which temperature equilibrates at a value appreciably below its peak value is for the lowest duty cycle under examination ($D = 10\%$). Herein can be clearly seen the competing effects of Joule heating and active cooling by the cold-cycle refrigerator. For this particular case (in which heating effects are more modest), the initial rapid temperature rise is eventually mitigated by the much slower cooling process. This important observation suggests that, for low duty cycles, FPA-detected signal strength may actually improve with increasing time after an initial reduction that is transient in nature (albeit not to the high signal level obtained when lasing is first initiated). At the other extreme ($D = 25\%$), cryostat temperature was found to monotonically increase for an appreciably longer period of time than lower duty cycles before reaching a steady-state value. Indeed, the time required to achieve thermal equilibrium was found to rise proportionally with the duty cycle under which the laser was operated.

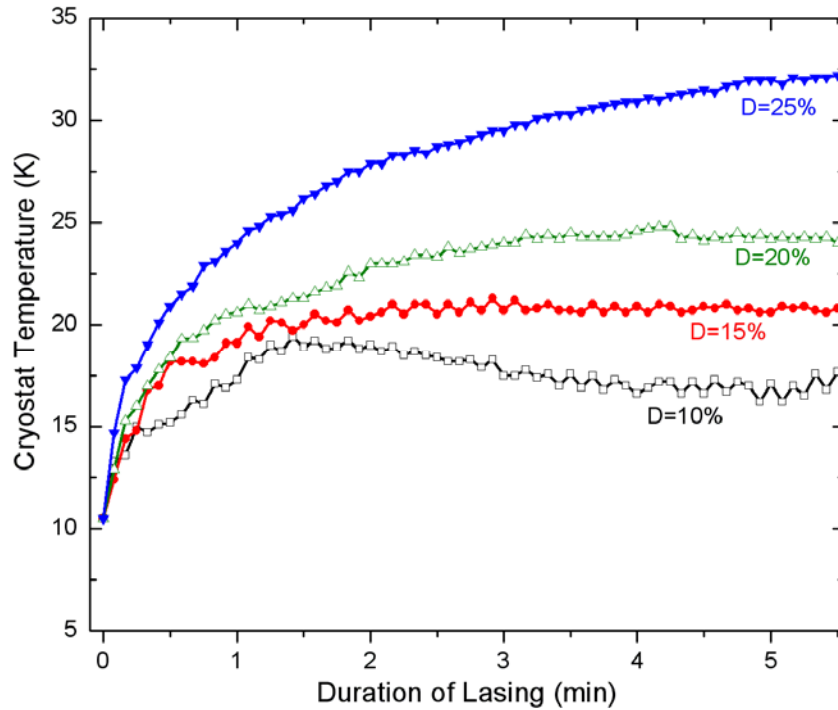


Fig. 21. Effects of duty cycle on laser performance: Signal intensity detected by FPA while operating QCL, at 300 kHz pulse rate and applied bias of 9.7-10.5 V, over extended period of time. (Cryostat set to 10 K.)

As predicted, these observed temperature changes are, in turn, responsible for a corresponding decline in QCL signal strength. Again, this is likely due to the reduced population inversion that results from thermal excitation of electrons between the quantized energy states of the laser. Fig. 22 quantifies the extent to which duty cycle affects laser beam intensity over extended periods of time. From these results, it is clear that QCL operation at a 25% duty cycle is fundamentally different from that produced using lower duty cycles. Temperature rises occur under each scenario. But, whereas signal intensity remains roughly constant in time for duty cycles of 10-20%, it drops precipitously (and immediately) for values above this range. In light of these observations, it can be posited that there is a threshold value of duty cycle, between 20% and 25%, above which the laser is no longer capable of serving as a useful terahertz imaging illumination source for more than a brief period of time.

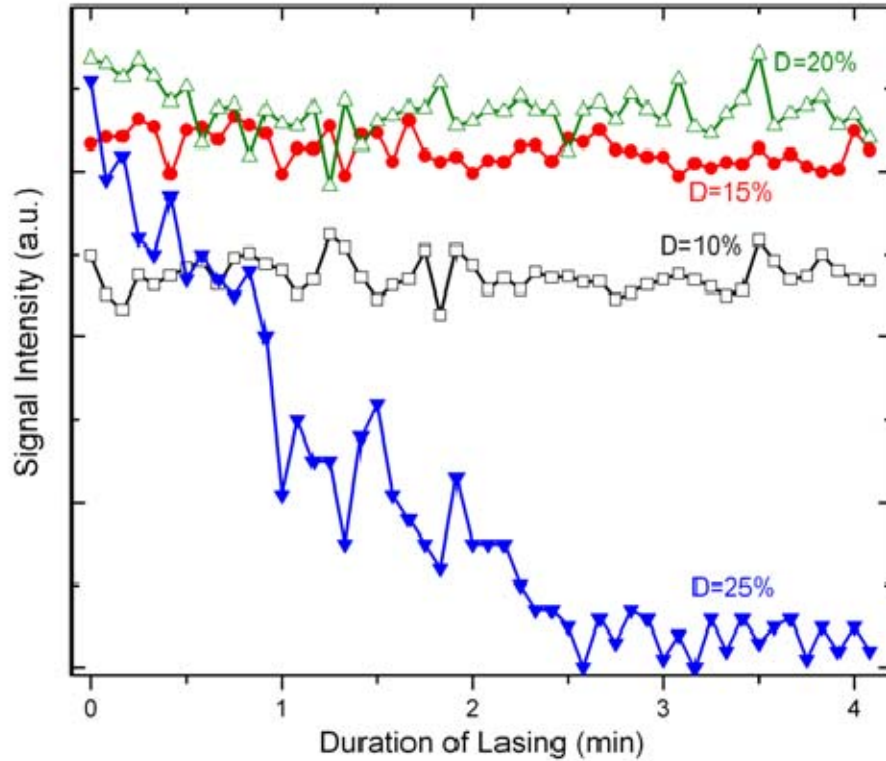


Fig. 22. Effects of temperature on laser performance for various duty cycles (D): Signal intensity detected by FPA while operating QCL, at 300 kHz pulse rate and applied bias of 9.7-10.5 V, over extended period of time. (Cryostat set to 10 K.)

These fundamentally distinct results can be explained by considering the magnitude of temperature change elicited by each scenario. At lower duty cycles, the relationship between cryostat temperature and duty cycle was found to be approximately linear (with slope of 0.6K/percent). For duty cycles above 20%, though, linearity of the relationship collapses and temperature of the laser assembly rises dramatically—nearly extinguishing the output beam entirely. As mentioned previously, this is likely due to thermally-activated electrons populating the lower laser level from the first conduction subband. During lasing at low temperatures, the lower laser level is depopulated via photon-phonon interactions; however, at elevated temperatures, this process is frustrated—preventing population inversion between the upper and lower laser levels.

In light of these findings, imaging experiments were conducted under different operating conditions, depending upon the type of detection desired. For single-frame images taken immediately after the commencement of lasing, large voltage bias and high duty cycle were used to produce a high-power (albeit short-lived) output beam. In general, though, these aggressive conditions were not found to produce an exceptionally superior output power. Furthermore, they would have little utility in any practical imaging system. As a result, most imaging—for both still frames and extended video recording—was performed under more modest operating conditions (typically 10-11 V applied bias, with 15-20% duty cycle.)

Fig. 23 provides further insight into the temporal behavior of QCL temperature during typical operation. When the QCL is first turned on with the application of an electrical bias (1.7 A in the present case), temperature rises, in logarithmic fashion, to a steady-state value over the course of several minutes. After removing the applied voltage bias, the sensor temperature drops rapidly (initially in linear fashion, at a rate of approximately 0.2 K/sec). Within roughly three minutes, the device returns to the 10 K temperature at which the chamber thermostat is set.

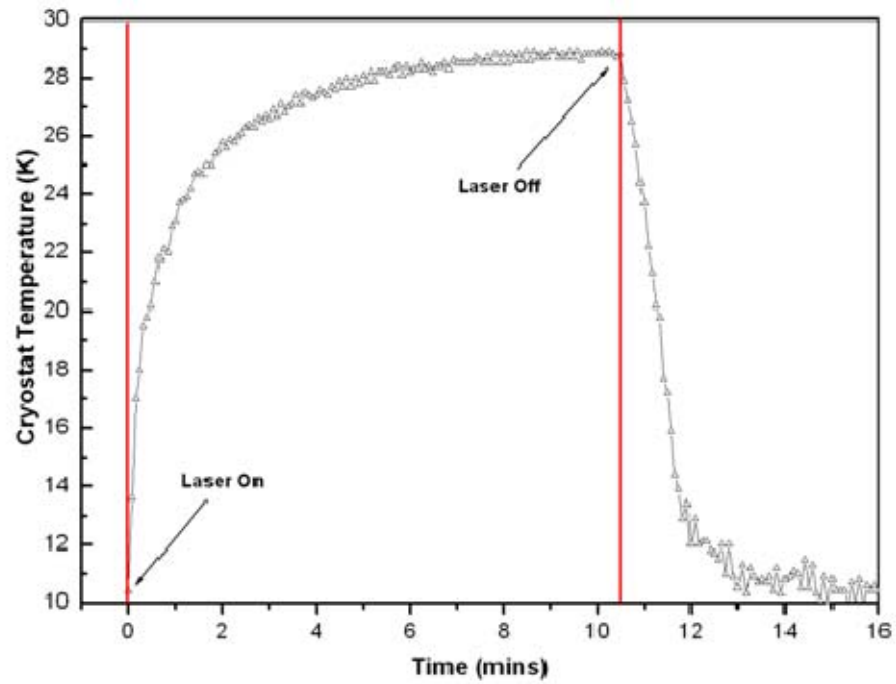


Fig. 23. Cryostat temperature changes arising from operation of the QCL at 20% duty cycle and applied bias of 10.4 V (1.7 A). Under these conditions, the cryostat reaches a steady-state temperature of 29 K after approximately eight minutes. Upon ceasing current flow to the laser, cryostat temperature drops at an approximate rate of 0.2 K/sec.

THIS PAGE INTENTIONALLY LEFT BLANK

VI. IMAGING RESULTS

The two QCLs used in these imaging experiments follow the same basic design principles and were fabricated using similar methods; however, the quality and persistence of imaging results yielded by the lasers differ dramatically. In general, results obtained using the 2.7-THz QCL as an illumination source were inferior in all respects to those produced using the 3.6-THz laser. Much of this deficiency appears to be directly attributable to the effects of elevated temperature on the laser, even though the rate of temperature rise for the two devices were roughly the same (from 10K to ~30K in 3-5 minutes). For instance, under nominal operating conditions, the 2.7-THz laser produced high-quality video imaging for a duration of 4-6 seconds; longer intervals of time rapidly produced a “wash-out” effect in which the beam was almost entirely extinguished and undetectable by the microbolometer system. The beam was again reproducible by cutting power from the device and waiting 5-10 minutes for the Joule heating in the laser to dissipate. Conversely, the 3.6-THz laser was capable of producing a consistent, high-intensity beam for extended periods of time (10 minutes or more).

Much of this disparity in the performance of the two laser devices can be understood by considering the relative energy gap produced by the multiple quantum well structure in the laser active region. As previously explained, both lasers operate off of a three-level lasing scheme within the conduction band; the effective energy gap exploited by the 2.7 THz laser and the 3.6 THz laser are 11 meV and 15 meV, respectively. This energy gap difference, which is more than 35% of the 11 meV value, is particularly significant when considering the fact that thermal population of the upper lasing level is exponentially increasing with temperature. At 300K, the Boltzmann factor for the 2.7-THz and 3.6-THz lasers are roughly equal, giving a ratio of electron populations for levels 3 and 2 (N_3/N_2) of about 0.65 and 0.56, respectively. At cryogenic temperatures, however, the difference in Boltzmann factor becomes much larger. At 10 K, for instance, N_3/N_2 for the 2.7-THz laser is more than a factor of 75 greater than that of the 3.6-THz QCL.

Imaging data produced using the 2.7-THz and 3.6-THz lasers demonstrate the significant value of having more than one terahertz laser available for this series of experiments. These data suggest that QCLs designed with higher resonant frequencies can, in general, be expected to produce superior illumination conditions for terahertz imaging. As corroborated by the quality of still and video images in the following two sections, this improvement is manifest in two ways. The most notable and important improvement is in the persistence of illumination during extended video imaging. However, it is evident that the higher-frequency QCL provides a slightly superior quality of single-frame images as well.

A. IMAGING AT 2.7 THz

Using the optical arrangement described above, imaging experiments were performed by inserting metallic objects, wrapped within various obscurants (plastic, paper, and cloth), roughly midway between the two parabolic mirrors such that a focused image fell on the microbolometer FPA. For single-frame imaging, the laser was typically operated at a 300 kHz repetition rate, a bias of 1.3-1.6 A, and 15% duty cycle. Fig. 24 is representative of the results obtained and demonstrates the methodology used to refine the image quality of a utility knife blade wrapped in opaque plastic tape (Fig. 24a). (One edge of obscuring tape was cut with a non-linear contour and notched so as to better identify orientation of the knife and facilitate evaluation of the system's imaging success.)

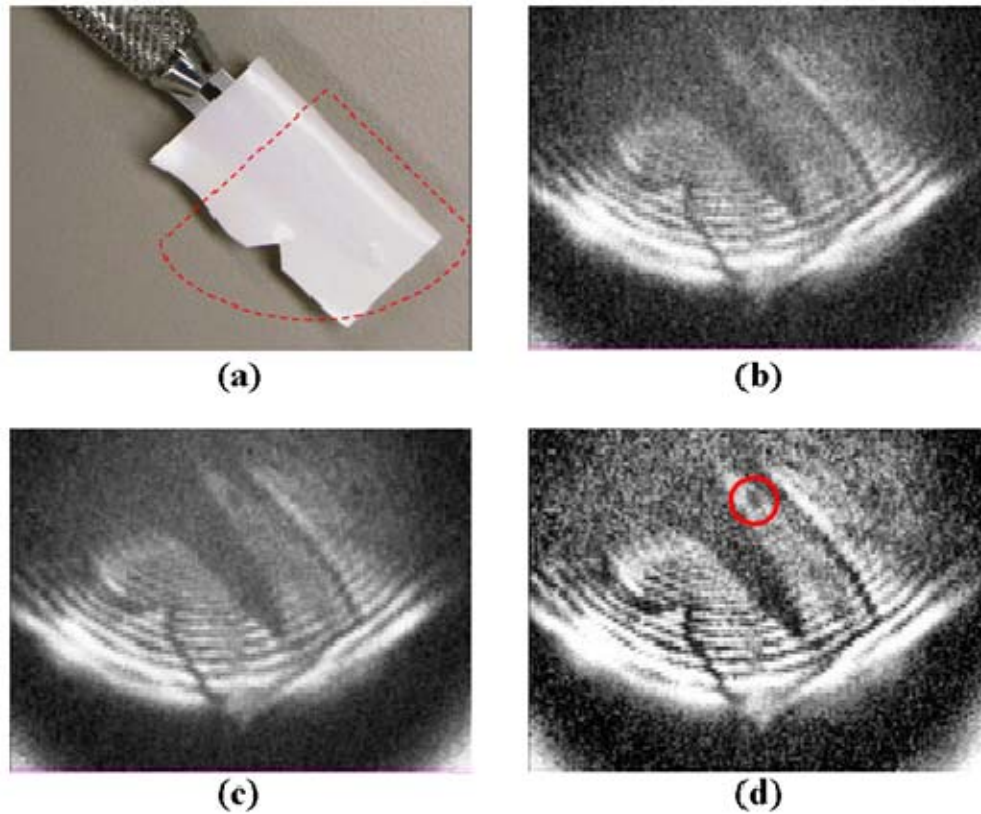


Fig. 24. Imaging of a small utility knife blade wrapped in opaque plastic tape. (a) Conventional digital photograph. Red dotted region represents approximate area of illumination. (b) Single frame image of blade assembly illuminated with 2.7-THz QCL radiation and imaged with microbolometer camera. (c) Image generated by computationally averaging 50 individual frames. (d) Fifty-frame composite image, refined using MATLAB image processing utility software. Orphan particle is visible within red circle.

Although single-frame images showed good contrast between the two objects (Fig. 24b), further improvements were achieved by taking multiple individual images of the stationary ensemble. When image averaging techniques are used to combine these frames into a composite image (Fig. 24c), noise effects are averaged out and overall clarity is improved. Finally, using noise reduction software applications, still greater contrast can be achieved (Fig. 24d). Fig. 24d was obtained by operating upon Fig. 24c with a series of MATLAB image processing algorithms: contrast-limited adaptive histogram equalization (CLAHE), decorrelation stretch with 5% tolerance saturation, and intensity adjustment with 1% saturation. The same imaging methodology is used for

imaging of a large paperclip in Fig. 25. Fig. 26 shows imaging results for three additional objects under similar optical conditions.

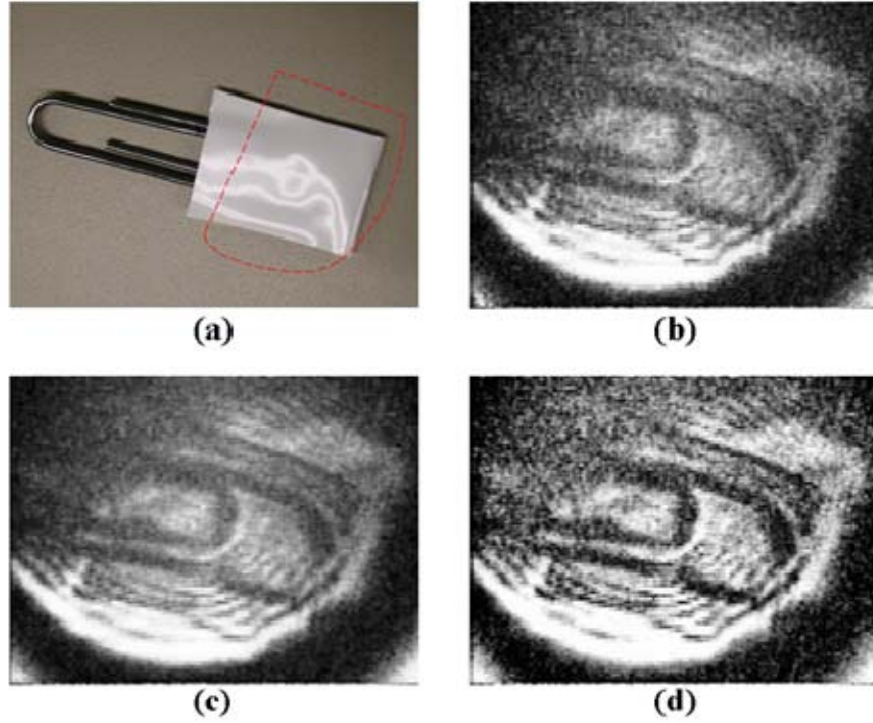


Fig. 25. Imaging of a large paper clip wrapped in opaque plastic tape. (a) Conventional digital photograph. Red dotted region represents approximate area of illumination. (b) Single frame image of blade assembly illuminated with 2.7-THz QCL radiation and imaged with microbolometer camera. (c) Image generated by computationally averaging 50 individual frames. (d) Fifty-frame composite image, refined using MATLAB image processing utility software.

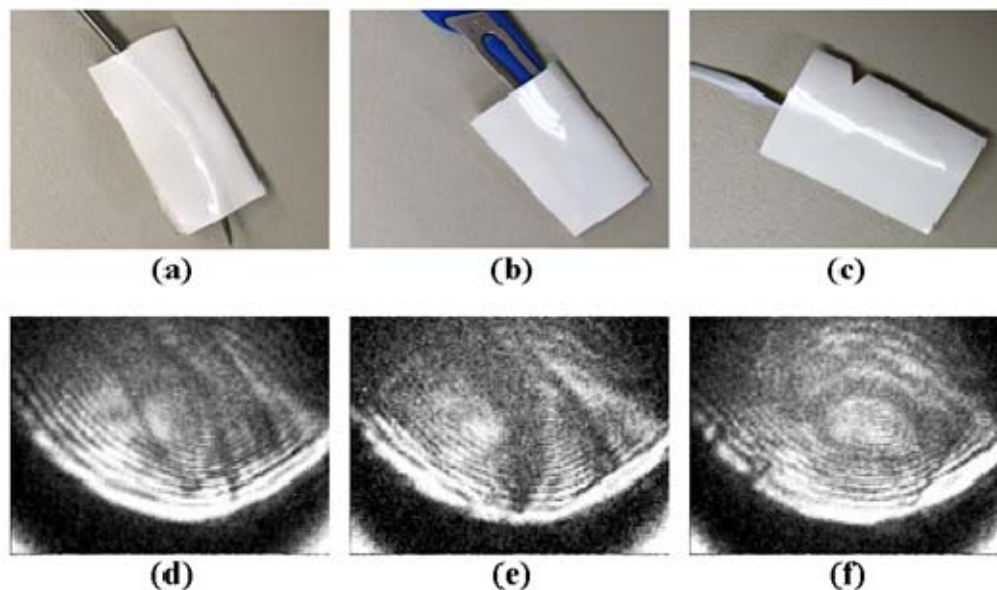


Fig. 26. Various objects, wrapped within two layers of opaque plastic tape, imaged using 2.7-THz QCL and microbolometer FPA. Upper images are conventional photographs taken with a compact digital camera; lower images are 50-frame averages of terahertz images enhanced with MATLAB noise reduction post-processing. (a, d). Dentist's pick. (b, e). Dissection scalpel with curved blade. (c, f). Plastic tie bent into a loop.

The advantage offered by image averaging and/or computer-based post-processing techniques is perhaps best appreciated by noting the small speck of (nonmetallic) foreign material which, having become accidentally embedded within the plastic tape, can be seen in terahertz images near the top of the illumination region (circled in Fig. 24d). In the unmodified single-frame terahertz image (Fig. 24b), the contaminant is barely distinguishable within the image's background noise. In Fig. 24c and Fig. 24d, however, it is clearly recognizable as a distinct object.

As previously mentioned, the primary limiting factor to this imaging arrangement is rapid heating of the laser due to Joule heating from the input current. Heating effects were mitigated by chopping the 300-kHz driving signal with a 20-Hz gating frequency and slow sweep rate to allow the device to cool intermittently. Due to its intermittent nature, such an illumination scheme is not useful for extended-duration imaging of moving objects. To allow imaging for several continuous seconds, the external gate

generator was disabled and input current and duty cycle of the input signal were both appreciably decreased (to roughly 0.93 A and 8%, respectively) to mitigate heating effects.

The results of video imaging with the 2.7-THz QCL are presented, in .avi format, in Fig. 27. Despite the resulting reduction in average laser power, real-time video recordings under these operating parameters are only slightly inferior to still-frame images. Although raw video was of acceptable quality, video filters (blur and box blur; sharpen, level and HSV adjustments) were applied to each of the four images to improve overall contrast.

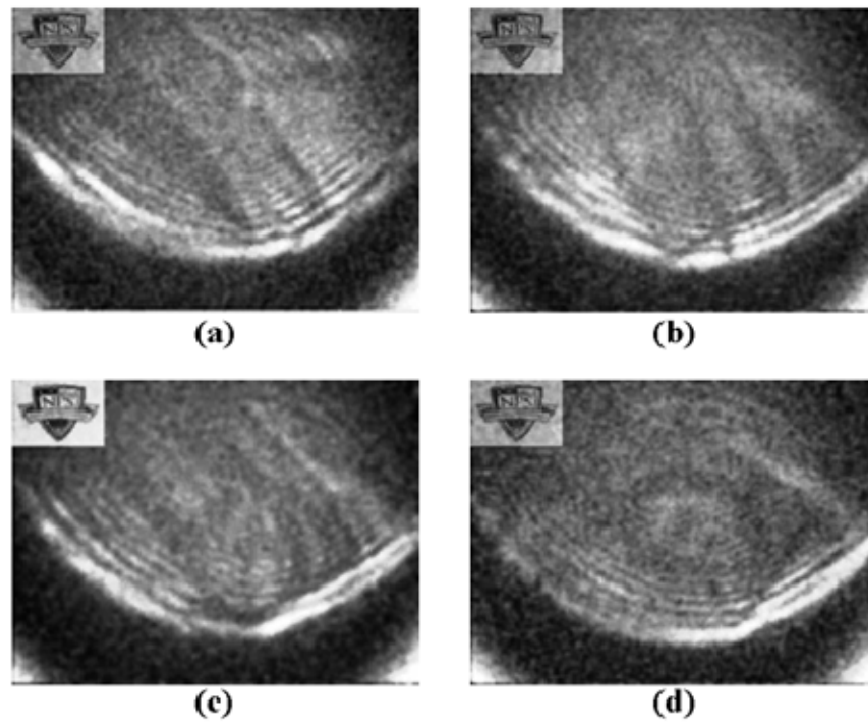


Fig. 27. Still images of video clips (with post-processing filters applied) from imaging experiments conducted using microbolometer FPA and 2.7-THz QCL operated at a 300 kHz pulse repetition rate, 8% duty cycle, and applied bias of 1.0 A. All objects were wrapped in two layers of opaque plastic tape. (a) Steel utility blade. (b) Dentist's pick. (c) Large paperclip. (d) Plastic tie bent into the shape of a wire loop.

Significant diffraction effects, produced by the influence of various system optics on the terahertz beam (QCL aperture diffraction, as well as etalon effects arising within the

Tsurupica lens and cryostat window), are apparent in the form of sharply-defined, concentric fringe patterns appearing throughout each of the terahertz images.

B. IMAGING AT 3.6 THz

Like those conducted at 2.7-THz, imaging experiments at 3.6-THz were performed with a 300-kHz PRF and a 30-Hz FPA frame rate. Due to its higher resonant frequency (and the correspondingly larger energy gap used for stimulated emission), however, the 3.6-THz QCL was able to tolerate higher temperatures and therefore operate effectively under more robust electrical conditions. For still-frame and extended video imaging alike, the laser was nominally operated with an applied bias of 1.6-1.9 A and a 15-20% duty cycle.

Fig. 28 is a collection of video clips demonstrating the type of real-time imaging that is obtainable under the aforementioned optical arrangement. All images were taken (using commercial frame grabber software) by the IR-160 microbolometer camera, at a 30-Hz frame rate, under illumination by the 3.6-THz QCL. The QCL was operated with a bias of 1.9 A at a 300-kHz pulse rate and 20% duty cycle.

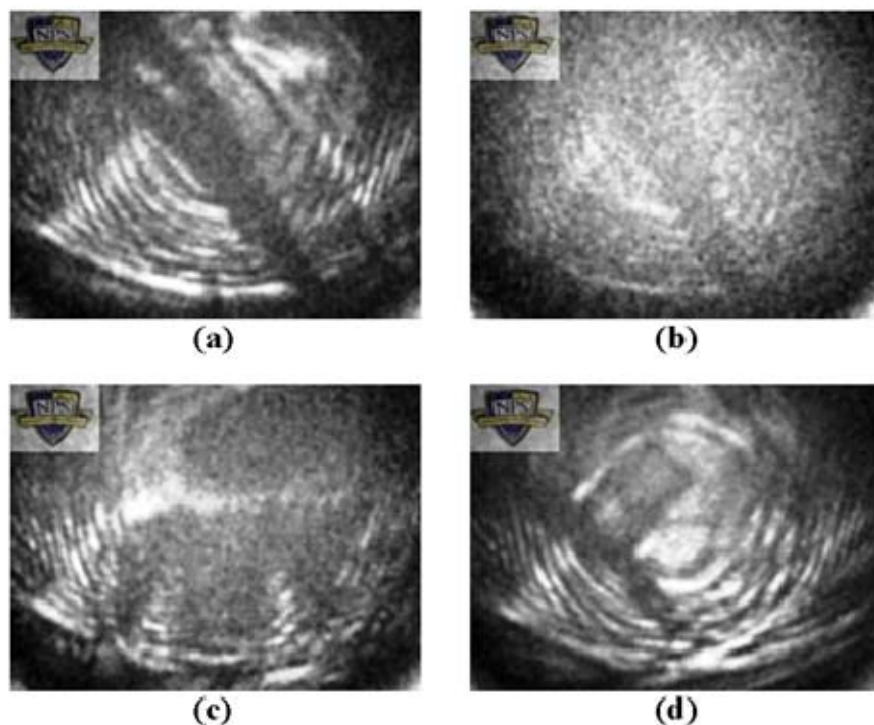


Fig. 28. Still images of video clips (with post-processing filters applied) from imaging experiments conducted using microbolometer FPA and 3.6-THz QCL operated at a 300 kHz pulse repetition rate, 20% duty cycle, and applied bias of 1.9 A. (a) Steel utility blade obscured by two layers of opaque plastic tape. (b) Utility blade concealed with common bond paper. (c) Mylar[®] film cut in the shape of the Ironman Triathlon[®] “M-Dot” logo and enclosed by two layers of opaque plastic tape. (d) Finger of a black polyurethane glove containing an Allen wrench, which in turn is wrapped with a small swatch of opaque plastic tape.

Interest in terahertz imaging is largely driven by the fact that, whereas terahertz radiation is strongly reflected by metals, it penetrates most non-metallic materials with little-to-no attenuation. This provides good image contrast between metals and obscurants of non-metallic constitution. As is seen in Fig. 28, the contrast is particularly striking in the case of plastic materials. Steel blades, such as the one imaged in Fig. 28(a), can be clearly seen when wrapped in opaque plastic tape—and remain visible even when enclosed by as many as eight layers of tape. To a lesser extent, metals are also detectable through cloth and common bond paper (Fig. 28(b)). Biaxially-oriented polyethylene terephthalate (boPET) film (more commonly known by the trade name Mylar[®]) was found to also strongly absorb terahertz radiation—even when used in

exceptionally thin quantities (Fig. 28(c)). Finally, it is noteworthy that this terahertz imaging scheme is also capable of imaging non-metallic materials within other non-metallic materials. In Fig. 28(d), the terahertz beam is sufficiently attenuated by both polyethylene and plastic tape that each material can be clearly distinguished from the other.

Fig. 29 contains another set of four images, taken under the same illumination scheme as in Fig. 28. Herein, more challenging sets of imaging conditions were investigated—demonstrating that available power from the QCL is somewhat inadequate for penetrating thicker obscurants. However, image resolution is still sufficiently robust so as to allow identification of the various objects. Furthermore, it is in such demanding imaging arrangements that the utility of image processing and/or color addition becomes apparent.^{††} In each of the four imaging samples represented within Fig. 29, video files were decomposed using VirtualDub (a video capture/processing application available for free use under the GNU General Public License) into a series of individual images; these images were then adjusted for contrast, brightness, and saturation level using a batch operation in Microsoft[®] Picture Manager to obtain optimal differentiation of the distinct objects under illumination. Final reassembly of the images was performed using VirtualDub. By employing this approach (video decomposition, image adjustment, and reconstitution), one obtains an improved level of editorial control over the quality and resolution of the original video file. Nevertheless, it should be emphasized that the final imaging product does not represent a dramatic improvement over the original video results; direct FPA video output still allows full differentiation of the objects of interest.

Fig. 29(a) is the now-familiar utility blade from previous images concealed behind a single layer of relatively thick (2 mm) Plexiglas. Fig. 29(b) demonstrates the strong terahertz attenuation associated with even thin layers of sponge-like foam packing material. In this image, an embedded 0.5-mm lead from a mechanical pencil is barely resolvable. Fig. 29(c) is extended video recording of terahertz imaging of a U.S. \$5 bill.

^{††} For the remainder of this thesis, for purposes of easy identification and categorization, red colorization is used in images of *objects* concealed within obscurants; blue colorization is used in images of paper-based materials directly illuminated by THz radiation.

Notable in this image are two types of government security (anti-counterfeit) features: a vertically-oriented narrow plastic thread (~ 1 mm in width) and an internal watermark of President Abraham Lincoln (3 mm long by 2 mm wide) on the left and right extremes of the bill, respectively. (Neither security feature is visible under normal observation; however, each can be detected when back-illuminated by a white light source.)

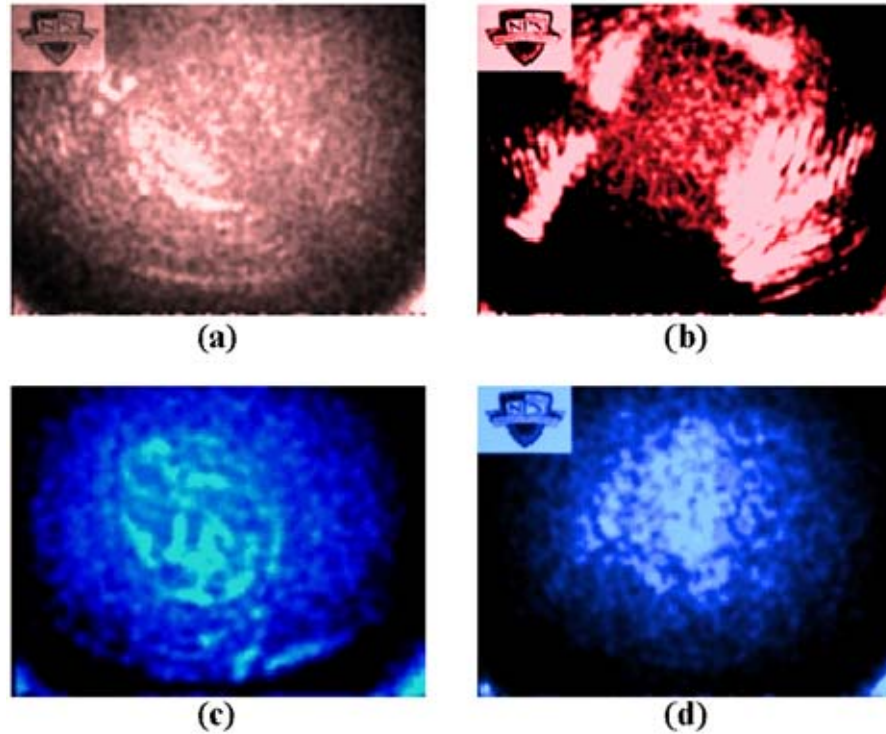


Fig. 29. Still images of video clips (with colorizing and post-processing filters applied) from imaging experiments conducted using microbolometer FPA and 3.6-THz QCL operated at a 300 kHz pulse repetition rate, 20% duty cycle, and applied bias of 1.9 A. (a) Steel utility blade obscured by a layer of Plexiglas. (b) mechanical pencil lead embedded in foam. (c) Watermark of President Abraham Lincoln from a U.S. \$5 bill (embedded video clip also includes imaging of plastic security thread). (d) “NPS” (“N” in still-frame image) written in number-two pencil, on a sheet of common bond paper.

Great Britain Pound (GBP) notes arguably contain some of the most robust security features of any currency in the world. For this (and other) reasons, it is also a superb choice for examination under terahertz imaging. For purposes of this research, a GBP £5 note was used as the imaging specimen. As with U.S. currency notes, British notes contain a watermark which (when using a conventional white light source) is only

visible under back-illumination (Fig. 30a). As seen in Fig. 30b, this watermark is clearly discernable in terahertz images as well. While the terahertz image does not contain the same level of detail and clarity produced by rear-illumination of visible light, it does potentially provide an additional layer of security against counterfeit practices by making watermark duplication more difficult (insofar as any attempt at watermark forgery would need to be visible under both imaging schemes).

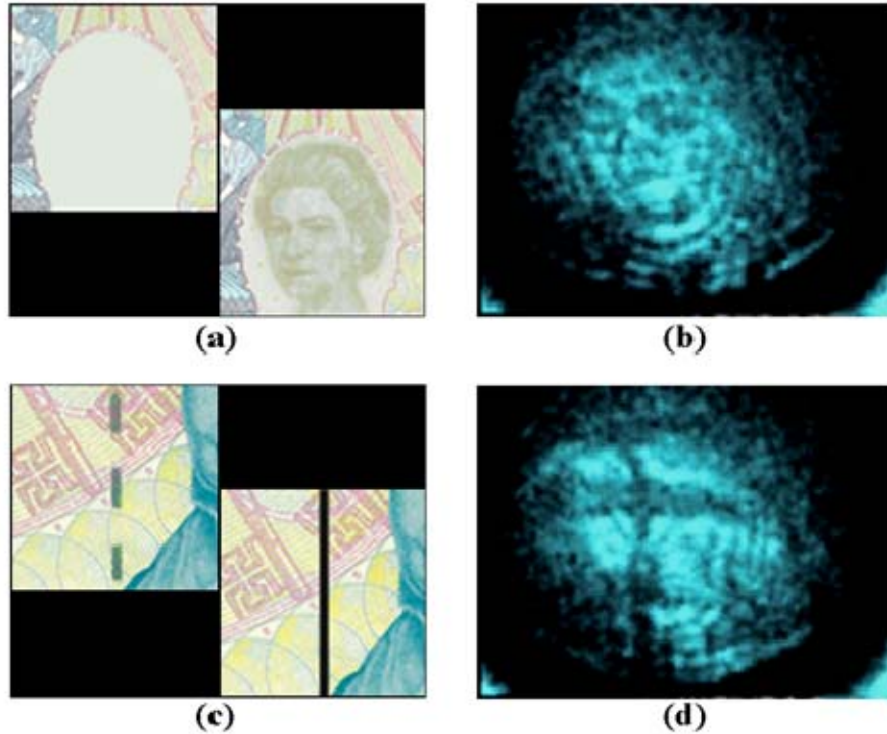


Fig. 30. £5 Great Britain Pound (GBP) note. (a) Watermark image of Queen Elizabeth II, as seen under illumination by forward-incident and rear-incident white light source (top-left and bottom-right corners, respectively). Only under the latter scheme is the watermark visible. (b) Terahertz imaging of watermark using microbolometer FPA and 3.6-THz QCL operated at a 300 kHz pulse repetition rate, 20% duty cycle, and applied bias of 1.9 A (with post-processing filters applied). (c) £5 security thread as seen under illumination by forward-incident and rear-incident white light source (top-left and bottom-right corners, respectively). (d) Terahertz imaging of security thread (using same operating parameters as in (b)). Notable in this animation is the elaborate *cross*-thread structure, a security feature which is relatively undetectable using white light sources.

More impressive is the ability of terahertz imaging to detect security features within GBP notes which are relatively undetectable under conventional white light illumination. British notes contain an internal security thread which is decidedly more

complex than U.S. currency. The thread (Fig. 30b), which appears as a dashed and solid line when viewed under illumination by forward-incident and rear-incident white light sources, respectively, also contains an elaborate cross-thread structure which is not immediately apparent, even with the highest levels of scrutiny, under visible light. As seen in Fig. 30d, terahertz imaging reveals that these cross-threads, which are remarkably elongated in the lateral dimension, appear at regular intervals along the entire length of the security thread. (The strong attenuation of terahertz radiation by these cross-stitches suggests that they are quite likely metallic in nature.) Were terahertz imaging to be adopted as a countermeasure against GBP forgery, an aspiring counterfeiter would be forced to produce internal threads which contain the same unique optical properties as this material (solid straight line under visible light; stitching under terahertz radiation)—a difficult prospect indeed. It is worth noting that the existence of this cross-thread feature is, to the best of the author’s knowledge, relatively obscure. No mention of it can be found in the public domain, even within banking and government web sites which purport to document the complete set of security features (some of which are only viewable under black or ultraviolet light) that are embedded into each nation’s currencies.

C. IMAGING AT 0.7-3.0 THz USING INTRACAVITY DFG

In the very final stages of this dissertation research (immediately after concluding a presentation at the 2008 Photonics West conference), the author was approached by Stanford University research professor Dr. Konstantin Vodopyanov with a very timely and promising opportunity for collaboration. Dr. Vodopyanov’s research group had recently developed a specific lasing scheme in which milliwatt-scale terahertz radiation is produced by applying difference frequency generation (DFG) techniques to a 1064-nm Nd:YVO₄ source laser [58]. Through the introduction of a quasi-phase-matched nonlinear crystal into the beam path (for the particular research effort cited here, periodically-poled lithium niobate (LiNbO₃) or GaAs crystals are used), an optical parametric oscillator (OPO) mechanism is produced in which the Nd:YVO₄ pump beam (with radial frequency of $\omega_p = 1.77 \times 10^{15}$ rads/sec) can be down-converted into two approximately-identical beams, of radial frequency ω_s and ω_i (corresponding to the signal

and idler beam, respectively). Plainly, conservation of energy requires that $\omega_s + \omega_i = \omega_p$. By judicious selection of the signal and idler frequencies, then, any frequency below that of the pump laser can (in theory) be produced by DFG of the two slave beams using nonlinear crystals. For the generation of terahertz radiation, the only critical requirement is that the signal and idler beams differ in frequency by that value desired for the DFG-produced beam. The specific process currently in use by Dr. Vodopyanov's group is doubly-resonant (both the signal and idler beams are produced and amplified within the cavity), near-degenerate (ω_s and ω_i are almost, but not quite, identical) parametric amplification. The particular frequency produced by the DFG scheme is determined solely by the refractive index of the nonlinear crystal, which can be controlled through adjustments in crystal temperature (these temperature shifts are produced through conduction effects arising from heating of the crystal on a thermal stage).

The proposed collaboration was realized on 29 Feb 2008, when NPS and Stanford researchers met and worked together in Ginzton Laboratory to conduct experiments involving the OPO and the IR-160 microbolometer camera. In these imaging trials, the IR-160 camera replaced the deuterated triglycine sulfate (DTGS) detector in the optical arrangement and used for detection of 3.02, 2.8, 2, and 0.7 THz output beams. Due to the frequency-mixing scheme employed, there is a strong infrared component (attributable to the $\sim 2\text{ }\mu\text{m}$ signal and idler beams) in the laser's virgin output signal. This component was effectively eliminated by including a Microtech low-pass filter, which has $\sim 100\%$ attenuation for the infrared components involved, into the beam path. The IR-160 was mounted (without the 20-mm Tsurupica lens used in the previous experiments) one focal length from a 50-mm Tsurupica lens used in the Stanford optical system. As seen in Fig. 31 and Fig. 32, these beams were imaged successfully. Although Fig. 31 is dominated by infrared contributions from the signal and idler beams, it does provide valuable insight into the quality of beam used for generation of the terahertz signal.

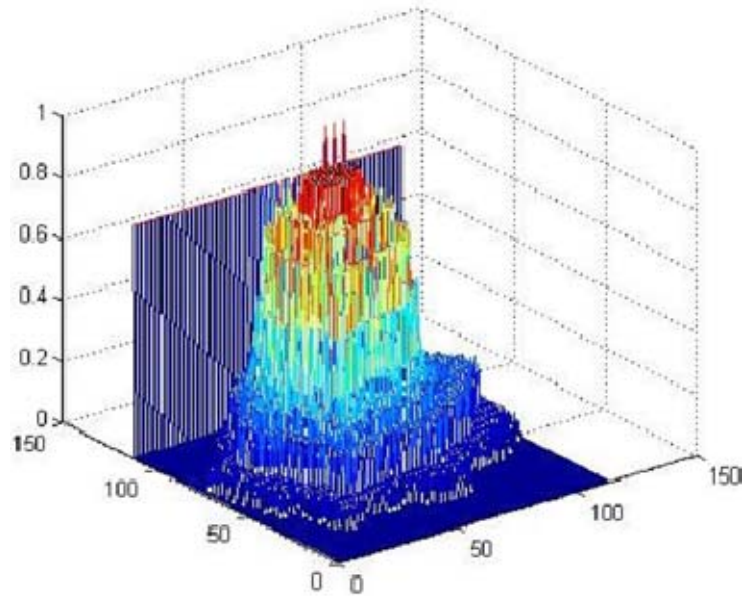


Fig. 31. Three-dimensional intensity map of the Stanford OPO laser beam during production of 2.8 THz radiation, as measured by IR-160 focal plane array (without low-pass filter). Due to the frequency-mixing scheme, beam intensity is predominantly attributable to the two $\sim 2\text{ }\mu\text{m}$ signal and idler beams.



Fig. 32. Colorized frame capture of IR-160 camera under illumination by 2.8 THz OPO beam (with Microtech lowpass terahertz filter included in beam path.)

The most noteworthy—if not surprising—product of these experiments involves examination of the 0.7-THz beam. Despite a relatively low signal-to-noise ratio, the 0.7 THz beam was successfully detected and imaged by the IR-160 camera. To the author's knowledge, this is the lowest frequency of radiation ever successfully detected using microbolometer technology—and suggests that microbolometer pixel membranes

remain absorptive at frequencies much lower than those for which they were designed. While confidence is high that the detected signal is indeed (and exclusively) the 0.7-THz radiation (and not the result of infrared beams bleeding through the low-pass filter), follow-up experiments are being designed that will enable the researchers to definitively confirm this conclusion.

THIS PAGE INTENTIONALLY LEFT BLANK

VII. POTENTIAL IMPROVEMENTS TO THE IMAGING SYSTEM

Having established the fundamental feasibility of real-time terahertz imaging using satisfactory but far-from-ideal components, the Sensors Research Group (SRG) has recently made sizable inroads towards further improving both the quality and compactness of a terahertz imaging system. This task has been approached from both source and the sensor perspectives. These include, most prominently, pursuing procurement of another, higher-power QCL from Jérôme Faist’s research group at the University of Neuchâtel, as well as the previously-mentioned collaborative opportunity with Stanford University. While average output power levels of the Stanford laser are currently inferior to the NPS QCL system, the Stanford laser exhibits remarkable tunability over terahertz frequencies (0.7-4.8 THz), and produces an output beam that is impressively “clean” (spot size is almost perfectly circular, and is not blemished by the fringing effects that are so pernicious in the NPS QCL). This latter characteristic is likely to be particularly valuable for imaging applications—especially for objects exhibiting fine detail, such as watermarks embedded within United States dollar (USD) or GBP notes. Fringing effects are little more than a minor liability when imaging bulk objects; however, images of objects containing print or fine detail are severely degraded by these diffraction-limited effects. Furthermore, the broad tunability of the Stanford laser provides an opportunity to more closely examine threshold detection limits of the microbolometer camera (determining high- and low-frequency cutoffs for the camera’s sensitivity). Finally, the Stanford laser operates successfully under room temperature conditions, obviating the current need for bulky and time-consuming cryogenic cooling equipment/processes and furthering the goal of developing a complete system (as opposed to only the sensor) that is capable of operating in a truly uncooled state.

A. DIFFRACTION EFFECTS

While not *critically* debilitating, the manifestation of diffraction effects acts to degrade overall resolution of the terahertz imaging system—particularly in the case of objects containing fine detail (e.g., images and/or text). Indeed, these effects currently

serve to classify the imaging scheme as a diffraction-limited system. These diffraction effects are principally driven by (1) the long wavelengths associated with terahertz radiation ($\sim 100\ \mu\text{m}$), (2) the extraordinarily small output aperture of the QCL ($14\ \mu\text{m} \times 200\ \mu\text{m}$), and the presence of multiple optical components along the full extent of the beam path. As the first of these conditions is, by definition, an unavoidable consequence of terahertz radiation, attention must be directed to consideration of the latter two conditions. Small aperture size is an inherent feature of QCLs and thus not controllable under the current imaging scheme; however, adoption of a new laser source that operates upon entirely distinct physical laws is one straightforward and reasonably accessible solution to this technical issue (a point which argues strongly in favor of aggressively pursuing collaboration opportunities with Stanford). The last of these conditions, the influence of optics elements, is currently being remedied through the procurement of a wedged cryostat window. By replacing the uniformly-thick (4-mm) window with a wedged window of 3° inclination, any fringes which arise due to etalon effects within the flat window should be completely eliminated. Eliminating diffraction effects associated with the other three lensing media is a more intractable prospect; experimentation has demonstrated that they are, in large measure, absolutely necessary for producing an acceptably focused image at the FPA. However, to the extent that the Tsurupica lens has been found to be responsible for a large proportion of the cumulative fringing phenomena, it is worthwhile to examine Tsurupica lenses of other diameters and focal lengths. These options are currently being investigated.

B. OUTPUT POWER

As is often the case with basic research, the principal goal of this dissertation work is one of feasibility demonstration: a theoretical and experimental demonstration that real-time terahertz imaging can be successfully performed with the use of uncooled microbolometer technology. Within this set of expectations, the results obtained here are both successful and promising—and offer solid proof that such an imaging approach is worthy of further investigation. However, it is undeniable that the low output laser power from the current terahertz source places rather stringent constraints upon the thickness

and nature of materials through which imaging can be performed—and constrains the conditions under which the microbolometer’s imaging capabilities can be tested. With less than one milliwatt of average power at 3.6 THz, metal concealed by approximately 4-mm of plastic opaque tape can be successfully imaged. But terahertz imaging will not be competitive with other security imaging techniques (e.g., x-ray backscatter) until it is capable of discerning objects through and within a wide range of thick non-metallic materials. Terahertz transparency for many such materials has already been demonstrated; however, even relatively minor electromagnetic attenuation can and does serve to dramatically decrease the amount of terahertz power falling upon the FPA. A higher laser output power is certain to increase the thickness (and quite likely the breadth) of materials through which metallic objects can be imaged. The SRG is currently exploring (through correspondence with Prof. Jérôme Faist, the acknowledged pioneer (and co-inventor) of QCL technology) the prospect of obtaining another, higher-power QCL for use in future research experiments.

Another potential solution to the problem of low laser power lies with transitioning to an entirely different laser device. There exists an important experimental niche that can be filled by a custom-designed, “tabletop”-size free electron laser (FEL). Despite the fact that various U.S. laboratories have free electron laser facilities that are available for use by academia, most such lasers do not have the pulse characteristics that allow imaging using microbolometer camera systems. Many systems are not capable of lasing in the terahertz regime; others are capable of high-power terahertz pulses, but with slow repetition rates and exceptionally short pulse widths that are not amenable to microbolometer detection.

An example serves to illustrate the problem associated with these pulse characteristics. The far-infrared FEL system at U.C. Santa Barbara is capable of lasing at 63-338 μm with a peak power of 1-6 kW per pulse [59]. With a specified pulse length of 1-20 μs and a pulse repetition frequency (PRF) of 0-7.5 Hz, the absolute upper limit of laser average output power is given by:

$$P_{avg} = P_{peak} \cdot t_{pulse} \cdot f_{PRF} = (6 \text{ kW})(20 \mu\text{s})(7.5 \text{ s}^{-1}) = 900 \text{ mW} \quad (23)$$

Although this average output power is roughly two orders of magnitude greater than that currently produced by the aforementioned QCLs, the characteristics of the pulse itself are almost entirely incompatible with real-time microbolometer detection. The device's voltage source, which is essentially an enormous Van de Graff generator, requires time to build a sufficient electric charge for each pulse; this is the limiting factor which is responsible for the slow PRF. Therefore, using this illumination source roughly reduces the effective frame rate of the camera fourfold: from 30 Hz to 7.5 Hz.

More importantly, microbolometer imaging effectiveness is compromised by the relationship between FEL pulse width ($t_{\text{pulse}} = 0.02 \mu\text{s}$), pulse period ($f_{\text{PRF}}^{-1} = 133 \text{ ms}$), and the time constant of the pixel absorptive membrane ($\tau = 10 \text{ ms}$). This time constant determines the rise time with which the focal plane array responds to incident photons. Within a given laser pulse, then, the incident power that is absorbed at any moment by the FPA is given by the expression:

$$P_{\text{abs}} = P_{\text{peak}} (1 - e^{-t/\tau}) \quad (24)$$

where t is measured from the start of an individual pulse packet and achieves its maximum at t_{pulse} , the total (temporal) pulse width. Because the pulse period is a full order of magnitude longer than the thermal time constant, the effects of each pulse are essentially identical and independent—that is, sufficient time elapses between pulses that total energy absorbed by the FPA pixels decays to negligible levels before the beginning of each successive pulse. Maximum laser power absorption occurs at the end of the pulse (at $t=20 \mu\text{s}$); for the laser and microbolometer specifications that have been given above, this yields a maximum absorbed power of 12.0 W. However, this is only 0.2% of the laser's peak output power and occurs for an exceptionally brief period of time—for a time period that is significantly shorter than the time constant of the detection system. The net effect of this short pulse width and slow PRF are evident when one calculates the average power which is actually absorbed by the microbolometer over extended periods of time (over one or more multiples of one pulse repetition interval):

$$P_{\text{abs}_{\text{avg}}} = f_{\text{PRF}} \int_0^{t_{\text{pulse}}} P_{\text{peak}} (1 - e^{-t/\tau}) dt = f_{\text{PRF}} (0.12 \text{ mJ}) = 0.9 \text{ mW} \quad (25)$$

It is readily seen that—despite its impressively high peak output power—the pulse characteristics of this particular FEL provides an average effective power that is no better than the QCLs under investigation. Further, as discussed above, this laser source also carries with it a slow PRF that limits the effective video frame capture rate to only 7.5 Hz.

The particular case cited here is not a unique one; most other U.S. FEL systems have beam characteristics which are similarly incompatible with microbolometers for terahertz imaging applications. Again, this incompatibility argues strongly for the need for relatively small FEL devices which can be operated anywhere within the 0.1-10 THz range (higher frequencies, especially those corresponding to atmospheric absorption “windows,” being preferable), at high average powers (on the order of a hundred milliwatts or more), with relatively high pulse repetition frequencies (tens or hundreds of kilohertz). Such a laser source would allow full exploitation of microbolometer detectors as an imaging camera; the two systems together could likely image metals concealed by thicker layers of materials already investigated (plastic, rubber, cloth, paper) and possibly allow imaging through “new” materials which have heretofore been opaque (i.e., ceramics, cardboard, etc).

C. COMPACTNESS

Much of the novelty and allure of this research derives from the fact that the terahertz detector is remarkably portable, is entirely free of cooling requirements, and is not dependent upon elaborate optical elements. Unfortunately, the same can emphatically *not* be claimed for the QCL source employed in these experiments. Although the laser itself is extraordinarily small, the logistical infrastructure required to support its operation is, for all practical purposes, prohibitively cumbersome. Not only does the laser require mounting in a stable laboratory environment, its cryogenic demands (cooling to nearly liquid helium temperatures) are likewise stringent (adding to the system’s already-large spatial footprint). Finally, because the QCL output beam exhibits such a broad divergence angle, multiple focusing elements are required to converge the radiation and produce a collimated beam for the camera. (The cryostat

window, the presence of which is an unavoidable consequence of inflexible cooling demands, adds an additional optical element to the system.) Not until this multi-level deficiency in compactness is resolved will a portable system be viable. Fortunately, the scientific and engineering communities are actively addressing this shortfall. Indeed, one such investigation is well underway at the Naval Postgraduate School. In a novel approach to the problem of terahertz source compactness, NPS's Prof. Andrés Larraza is currently designing and fabricating MEMS-based, terahertz-tuned micro-magnetrons [60]-[61]. Conventional magnetrons (such as those used to generate microwaves) have physical dimensions which are excessively large for producing terahertz radiation; typical resonant frequencies for magnetrons are roughly 200 MHz. Scaling issues can be eliminated by adopting a smaller magnetron structure through MEMS fabrication techniques (thus securing a much smaller radius of curvature for electron acceleration); however, other technical issues remain. Although maximum magnetron frequency scales linearly with applied magnetic field according to the Larmour formula,

$$f_H = \left| \frac{e B}{4 \pi m_e} \right|, \quad (26)$$

there are practical limitations to the magnitude of magnetic field that can be sustained with such a device. In the case of conventional magnetrons, an extraordinarily powerful field (approximately 25 T) would be required to generate radiation at 1 THz; application of such a field would almost certainly result in an immediate structural failing of the magnetron. However, by employing a so-called “reverse magnetron” design (in which the polarity of the magnetron elements are reversed—such that the cathode constitutes the outer ring; the anode, the central cylinder—a terahertz-resonant cavity can indeed be technically feasible [60]. Successful realization of this source technology, if combined with the microbolometer detector reported herein, could result in a terahertz imaging system that is significantly more compact than any of the real-time systems currently in use.

D. TERAHERTZ-TUNED MICROBOLOMETER DESIGN

Having stipulated these caveats of this system's technical limitations, it is likewise important to recognize that nearly all of the technical weaknesses/issues associated with the imaging "system" (i.e., low power, fringing effects arising from optical diffraction, cooling requirements, bulkiness) are liabilities tied to the QCL source—not the sensor. To the extent that this research has been primarily concerned with the detection mechanism of a potential imaging system, these limitations are of only secondary importance to the investigation at hand. Nevertheless, there exist one notable (albeit highly work-intensive) opportunity to improve upon microbolometer performance, thus optimizing its sensitivity to terahertz radiation: re-engineering of the MEMS design.

There exist two principal reasons that conventional microbolometer technology is not well-suited for imaging at terahertz frequencies. The first is one of physical scale. Most IR-tuned microbolometer arrays are comprised of pixels with a 50- μm pitch (that is, they have square dimensions of $50 \times 50 \mu\text{m}^2$). Given that terahertz wavelengths are on the order of 100 μm ($\sim 3 \text{ THz}$), it is plain that pixel pitch should be increased to fully accommodate the wavelength disparity between IR and terahertz radiation. This size scales linearly with the wavelength ratio, such that a $\lambda=100 \mu\text{m}$ ("terahertz-tuned") pixel should have pitch distance that roughly 5-10 times that of a $\lambda = 8\text{-}12 \mu\text{m}$ ("IR-tuned") pixel. This increase would necessitate increasing the pixel length/width dimensions from 50 μm to 250-500 μm . Furthermore, care must be taken in re-engineering the depth of the array for such wavelengths. This is because most microbolometer pixel designs tightly engineer the separation distance (typically to one-half the design wavelength) between absorbing and substrate layers of the pixel so as to induce a "cavity" effect at IR wavelengths (thus optimizing pixel absorption of the incident radiation). However, in the case of a terahertz-tuned pixel, it is not feasible to engineer a cavity gap on the order of 40 μm ; therefore, one must use other criteria for determining the optimal depth of the sensor channel.

The second—and more important—element of microbolometer design ill-matched to the terahertz regime is that of the pixel membrane. Due to the high TCR of

vanadium oxide (VO_x) and strong absorption of infrared radiation by silicon nitride (Si_3N_4), a composite film of these two materials is used as the default membrane material used for IR-tuned microbolometers [55]. And, as this research has certainly borne out, the membrane remains at least partially absorptive in the terahertz regime. However, despite the fact that Si_3N_4 absorption has not been well-characterized at terahertz frequencies, computational modeling performed by Hu et al indicates that emissivity of the pixel membrane at 4.3 THz may be as low as 4% [36]. In light of the imaging results presented within this dissertation, this emissivity value seems suspiciously low (such low absorption would almost certainly be incapable of supporting the high-contrast imaging reported herein). However, it does support the premise that microbolometer operation could be significantly improved by adopting a different material for use in the membrane film. Identifying a candidate material that exhibits strong terahertz absorption is, in itself, a rather complicated prospect; despite the rapid pace of current research into terahertz-based technology, published papers on this area of material characterization are relatively few in number. A large proportion of the research that has been conducted into this field has been performed by the Submillimeter-Wave Technology Laboratory (STL) at the University of Massachusetts–Lowell, which specializes in investigations of 0.1–5.0 THz [62]–[65]. The STL has measured high terahertz absorption coefficients for Rexolite™ (a polystyrene plastic exhibiting 60% absorption at 6.3 THz [63]), hot-pressed hexagonal boron nitride (a polycrystalline material, used frequently as an insulating film for metal-insulator-superconductor (MIS) structures, with 90% absorption at 3.5 THz [64]), and various dichroic filters, produced using photolithographic techniques, that are currently in use as spectral bandpass filters for the terahertz regime and exhibit nearly 100% absorption above 450 GHz [65]. Some insight into the problem of material selection can also be gleaned from the imaging data presented in this dissertation. For instance, insofar as this research has clearly demonstrated that boPET film (such as that shown in Fig. 28) is capable of almost complete attenuation of terahertz radiation, Mylar®-type films could potentially serve this pixel function as well.

Unfortunately, even materials demonstrating near-perfect terahertz absorption are not necessarily amenable to microbolometer pixel design. While flexibility in choice of

material and thickness for MEMS fabrication is continually improving, the current state of MEMS production techniques is such that only a relatively modest range of materials are available for fabrication of such devices. This restriction serves to eliminate more exotic materials from pixel membrane candidates. Still, the exceptionally strong attenuation of terahertz radiation by nearly all metal types suggests that basic metallic materials (e.g., gold, which has widespread and well-established use in MEMS devices, and can be applied in a variety of thicknesses) may ultimately serve as a viable choice of pixel membrane medium. (The only immediately apparent disadvantage of this approach is the fact that metals have rather low TCRs (i.e., on the order of 0.002 /K, versus -0.023 /K for VO_x)

E. RECENT IMPROVEMENTS IN MICROBOLOMETER-BASED DETECTOR TECHNOLOGY

Very recently, Professor Karunasiri's Sensors Research Group has purchased a Thermoteknix Miricle 110 KS infrared (microbolometer) camera for further improvement in terahertz detection capability. Notable features of this system (as compared to the Infrared Solutions IR-160 camera) include nearly a six-fold improvement in total pixel count (384×288 array), a smaller pixel pitch (35×35 μm² versus 50×50 μm²), and a 100% improvement in NETD for passive, room-temperature imaging in the infrared regime (50 mK vs 100 mK). Additionally, the camera is capable of faster data collection (7 ms response time and 60-Hz frame rate, in contrast to 12 ms and 30-Hz for the IR-160, respectively). The pixel membrane material used in the 100 KS is not publicly known (it is considered company-sensitive information); however, it has a design absorptive range (7-12 μm) that is slightly more shorter than the 8-14 μm wavelength range that characterizes the IR-160. It is also capable of automatically outputting images in the form of a colorized intensity map, which may provide better contrast between (and, thus, differentiation of) multiple objects that are grouped, overlapped, or concealed within each other.

By all indications, this new camera system should support a measurable improvement in the SRG's terahertz imaging capability. Indeed, preliminary experiments

confirm that the focal plane array is markedly more sensitive to the QCL's 3.6 THz illumination than its predecessor. Direct terahertz illumination of the focal plane array, in the absence of the Tsurupica focusing lens, produces a noticeably brighter signal pattern than was found for the previous detector (Fig. 33). At the time of this writing, the most challenging engineering obstacle remains one of optics—successfully integrating the Tsurupica focusing substrate into the camera to produce a seamless detection system. For optimal performance, the lens must be integrated into the camera system with a lens assembly that (1) mates well with the external architecture of the camera device, and (2) allows sufficient travel of the Tsurupica element for manual focusing purposes. This integration has been accomplished with success in the IR-160 camera, but is still underway in the Thermoteknix system.

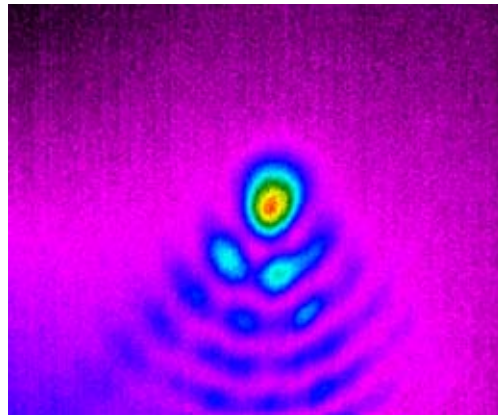


Fig. 33. FPA output from Thermoteknix Miricle 110K thermal imager, under illumination by 3.6 THz QCL output beam. The frame shown here makes use of the camera's contour plotting feature, in which varying levels of signal intensity are represented by a range of colors from blue (high intensity) to red (low intensity).

The SRG is currently working on parallel initiatives to (1) incorporate the aforementioned 20-mm Tsurupica lens into the camera and (2) commissioning production of a second, custom-designed Tsurupica lens (with longer focal length) from Microtech Instruments, Inc. Once completed and fully investigated using experimental methods, these improvement efforts are expected to yield a noticeable enhancement in image fidelity.

VIII. CONCLUSIONS

The research presented in this dissertation represents an early but critical step toward the realization of a highly robust terahertz imaging system. With the important exception of parallel, simultaneous, and completely independent investigations by Prof Hu's MIT group, it also represents the *only* research into the use of microbolometers as a terahertz detection mechanism. Two features of this imaging approach—real-time signal detection and uncooled operation—constitute major advantages over the currently-adopted techniques that have achieved relatively broad use throughout academia and industry. As such, microbolometer-based terahertz imaging is a research niche certainly worthy of further examination. In the author's opinion, further work in this area should be pursued aggressively—as should opportunities for academic collaboration with other researchers.

Imaging data presented here confirm the expectation that the strong attenuation of terahertz radiation by metallic objects and weak attenuation by nonmetallic objects can be exploited to address many important homeland security needs vis-à-vis imaging technology. Moreover, by examining a large range of nonmetallic materials, this research has more definitively identified the relative ease with which those materials can be imaged. To wit, it has been shown that plastics, rubbers, thin paper, and some fabric materials exhibit limited terahertz attenuation and are therefore ideally suited for terahertz imaging. In contrast, ceramics, foams, thick paper and heavier fabrics prove difficult media for terahertz beam transmission at low output powers. It is further noteworthy that surprising analytical results have been obtained while imaging domestic and foreign currencies (in particular, the heretofore unreported cross-stitch features embedded within GBP security threads). These suggest that, in addition to medical and homeland security applications, terahertz radiation may hold promise as an anti-counterfeiting technology.

Ultimately, a more versatile and portable laser source will be a necessary element of any successfully-integrated terahertz imaging system. Given the current state of

research into this area, however, more cumbersome sources (such as the QCL reported here) will have to suffice for some time in support of basic terahertz imaging research. In light of this, the above-detailed evaluation and refinement of techniques for optimizing both output power and quality of the NPS QCL beam have considerable value. It is the author's hope that they will serve as a useful operator's guide for optimizing QCL output in future imaging experiments.

Perhaps one of the most important results from the above research is the clear revelation that relatively low laser power is more than sufficient for basic terahertz imaging applications. The results obtained using milliwatt-scale laser power (which is, incidentally, the lowest average power ever reported in microbolometer-based detection experiments; roughly one-fiftieth of the power used in comparable studies by Hu et al [36]), holds important implications for similar studies in the future. It confirms that (1) high terahertz power is *not* a prerequisite for imaging success, and, by logical extension, (2) given the (eventual) luxury of higher laser powers, much better imaging resolution and fidelity should be achievable than was previously expected.

It would appear, in light of this and many other ongoing experimental investigations of terahertz imaging and spectroscopy, that the whimsically-titled "terahertz gap" may soon be populated with an array of realized applications. It has been soundly demonstrated that many of these applications can be effectively met through the use of microbolometer technology. From straightforward imaging of concealed objects, to the novel discovery that terahertz radiation can be used to detect heretofore "hidden" currency features, to the revelation that low-power laser sources are sufficient for realizing each of these important functions, the research presented in the above pages confirms that microbolometer-based detection of terahertz radiation holds great scientific promise. And, further, that it can provide a viable pathway towards further strengthening our national and personal security infrastructure.

LIST OF REFERENCES

- [1] D. Arnone, C. Ciesla, and M. Pepper, "Terahertz imaging comes into view," *Physics World* **4**, 35-40 (2000).
- [2] D. M. Mittleman, M. Gupta, R. Neelamani, R. G. Baraniuk, J. V. Rudd, and M. Koch, "Recent advances in terahertz imaging," *Appl. Phys. B* **68**, 1085-1094 (1999).
- [3] S. Hunsche, M. Koch, I. Brener, and M. C. Nuss, "THz near-field imaging," *Opt. Comm.* **150**, 22-26 (1998).
- [4] B. B. Hu and M. C. Nuss, "Imaging with terahertz waves," *Opt. Lett.* **20**, 1716-1717 (1995).
- [5] E. N. Grossman, A. Luukanen, and A. J. Miller, "Terahertz active direct detection imagers," *Proc. SPIE* **5411**, 68-77 (2004).
- [6] H.-T. Chen, R. Kersting, and G. C. Cho, "Terahertz imaging with nanometer resolution," *Appl. Phys. Lett.* **83**, 3009-3011 (2003).
- [7] Q. Chen, Z. Jiang, G. X. Xu, and X.-C. Zhang, "Near-field terahertz imaging with a dynamic aperture," *Opt. Lett.* **25**, 1122-1124 (2000).
- [8] D. Zimdars and J. S. White, "Terahertz reflection imaging for package and personnel inspection," *Proc. SPIE* **5411**, 78-83 (2004).
- [9] P. Y. Han, G. C. Cho, and X.-C. Zhang, "Time-domain transillumination of biological tissues with terahertz pulses," *Opt. Lett.* **25**, 242-244 (2000).
- [10] K. J. Siebert, T. Löffler, H. Quast, M. Thomson, T. Bauer, R. Leonhardt, S. Czasch and H. G. Roskos, "All-optoelectronic continuous wave THz imaging for biomedical applications," *Phys. Med. Biol.* **47**, 3743-3748 (2002).
- [11] T. Löffler, T. Bauer, K. Siebert, H. Roskos, A. Fitzgerald, and S. Czasch, "Terahertz dark-field imaging of biomedical tissue," *Opt. Express* **9**, 616-621 (2001).
- [12] X-C Zhang, "Terahertz wave imaging: horizons and hurdles," 2002 *Phys. Med. Biol.* **47** 3667-3677 (2002).
- [13] A. J. Fitzgerald, E. Berry, N. N. Zinovev, G. C. Walker, M. A. Smith and J. M. Chamberlain, "An introduction to medical imaging with coherent terahertz frequency radiation," *Phys. Med. Biol.* **47**, R67-84 (2002).

- [14] R. H. Clothier and N. Bourne, "Effects of THz exposure on human primary keratinocyte differentiation and viability," *J. Biol. Phys.* **29**, 179-185 (2003).
- [15] K. Humphreys, J. P. Loughran, M. Gradziel, W. Lanigan, T. Ward, J. A. Murphy, C. O'Sullivan, "Medical applications of terahertz imaging: a review," in *Proc. of the 26th Annu. Int. Conf. of the IEEE* (IEEE, 2004), pp. 1302-1305.
- [16] B. Ferguson, S. Wang, D. Gray, D. Abbott and X. -C. Zhang, "Identification of biological tissue using chirped probe THz imaging," *Microelectron. J.* **33**, 1043-1051 (2002).
- [17] J. Nishizawa, T. Sasaki, K. Suto, T. Yamada, T. Tanabe, T. Tanno, T. Sawai and Y. Miura, "THz imaging of nucleobases and cancerous tissue using a GaP THz-wave generator," *Opt. Commun.* **244**, 469-474 (2005).
- [18] J. E. Bjarnason, T. L. J. Chan, A. W. M. Lee, M. A. Celis, and E. R. Brown, "Millimeter-wave, terahertz, and mid-infrared transmission through common clothing," *Appl. Phys. Lett.* **85**, 519-521 (2004).
- [19] F. De Lucia, "Noise, detectors, and submillimeter-terahertz system performance in nonambient environments," *J. Opt. Soc. Am. B* **21**, 1273-1279 (2004).
- [20] J. F. Federici, B. Schulkin, F. Huang, D. Gary, R. Barat, F. Oliveira, and D. Zimdars, "THz imaging and sensing for security applications—explosives, weapons and drugs," *Semicond. Sci. Technol.*, **20**, S266-S280 (2005).
- [21] K. Kawase, Y. Ogawa, Y. Watanabe, and H. Inoue, "Non-destructive terahertz imaging of illicit drugs using spectral fingerprints," *Opt. Express* **11**, 2549-2554 (2003).
- [22] J. F. Federici, D. Gary, R. Barat, and D. Zimdars, "THz standoff detection and imaging of explosives and weapons," *Proc. SPIE* **5781**, 75-84 (2005).
- [23] J. O'Hara and D. Grischkowsky, "Synthetic phased-array terahertz imaging," *Opt. Lett.* **27**, 1070-1072 (2002).
- [24] Z. Jiang and X.-C. Zhang, "Single-shot spatiotemporal terahertz field imaging," *Opt. Lett.* **23**, 1114-1116 (1998).
- [25] K. J. Siebert, H. Quast, R. Leonhardt, T. Löffler, M. Thomson, T. Bauer, H. G. Roskos, and S. Czasch, "Continuous-wave all-optoelectronic terahertz imaging," *Appl. Phys. Lett.* **80**, 3003-3005 (2002).

- [26] J. Darmo, V. Tamosiunas, G. Fasching, J. Kröll, K. Unterrainer, M. Beck, M. Giovannini, J. Faist, C. Kremser, and P. Debbage, "Imaging with a terahertz quantum cascade laser," *Opt. Express* **12**, 1879-1884 (2004).
- [27] T. Kleine-Ostmann, P. Knobloch, M. Koch, S. Hoffmann, M. Breede, M. Hofmann, G. Hein, K. Pierz, M. Sperling, K. Donhuijsen, "Continuous-wave THz imaging," *Electron. Lett.* **37** 1461-1463 (2001).
- [28] Z. Jiang and X.-C. Zhang, "Terahertz imaging via electrooptic effect," *IEEE Trans. on Microwave Theory and Techniques* **47**, 2644-2650 (1999).
- [29] T. D. Dorney, J. L. Johnson, J. Van Rudd, R. G. Baraniuk, W. W. Symes, and D. M. Mittleman, "Terahertz reflection imaging using Kirchhoff migration," *Opt. Lett.* **26**, 1513-1515 (2001).
- [30] B. Ferguson, S. Wang, D. Gray, D. Abbot, and X.-C. Zhang, "T-ray computed tomography," *Opt. Lett.* **27**, 1312-1314 (2002).
- [31] A. Dobroiu, M. Yamashita, Y. N. Ohshima, Y. Morita, C. Otani, and K. Kawase, "Terahertz imaging system based on a backward-wave oscillator," *Appl. Opt.* **43**, 5637-5646 (2004).
- [32] M. S. Shur and V. Ryzhii, "New concepts for submillimeter-wave detection and generation," *Proc. 11th GaAs App. Symp.* 301-304 (2003).
- [33] I. S. Gregory, W.R. Tribe, B.E. Cole, C. Baker, M. J. Evans, I. V. Bradley, E. H. Linfield, A. G. Davies, and M. Missous, "Phase sensitive continuous-wave THz imaging using diode lasers," *Electron. Lett.* **40**, 143-145 (2004).
- [34] G. Karunasiri, "Real time THz camera using microbolometer focal plane array," presented at the 7th Int. Conf. on Technol. & the Mine Problem, Monterey, CA, 2-4 May 2006.
- [35] A. W. M. Lee, and Q. Hu, "Real-time, continuous-wave terahertz imaging by use of a microbolometer focal-plane array," *Opt. Lett.* **30**, 2563-2565 (2005).
- [36] A. W. M. Lee, B. S. Williams, S. Kumar, Q. Hu, and J. L. Reno, "Real-time imaging using a 4.3-THz quantum cascade laser and a 320×240 microbolometer focal-plane array," *IEEE Photon. Tech. Lett.* **18**, 1415 (2006).
- [37] M. Lowe, *Imaging of 3.4 THz Quantum Cascade Laser Beam using Uncooled Microbolometer Camera*, M.S. thesis, Naval Postgraduate School, Dec. 2006.

- [38] B. N. Behnken, M. Lowe, G. Karunasiri, D. R. Chamberlin, P. R. Robrish, and J. Faist, "Detection of 3.4 THz radiation from a quantum cascade laser using a microbolometer infrared camera," *Proc. SPIE* **6549**, 65490C (2007).
- [39] B. N. Behnken, G. Karunasiri, D. R. Chamberlin, P. R. Robrish, and J. Faist, "Use of 2.7-THz quantum cascade laser and microbolometer camera for imaging of concealed objects," in *Proc. of the 9th Int. Conf. on Intersubband Transitions in Quantum Wells*, D. Indjin, Z. Ikonic, P. Harrison, and R. W. Kelsall, ed. (University of Leeds, U.K., 2007).
- [40] B. N. Behnken, G. Karunasiri, D. R. Chamberlin, P. R. Robrish, and J. Faist, "Optimization of a 3.6-THz quantum cascade laser for real-time imaging with a microbolometer focal plane array," *Proc. SPIE* **6893**, 6893-22 (2008).
- [41] B. N. Behnken, G. Karunasiri, D. R. Chamberlin, P. R. Robrish, and J. Faist, "Real-time imaging using a 2.8 THz quantum cascade laser and uncooled infrared microbolometer camera," *Opt. Lett.* **33**, 440-442 (2008).
- [42] P. W. Kruse, *Uncooled Thermal Imaging: Arrays, Systems, and Applications*, SPIE Press, Bellingham, 2002.
- [43] Advanced Photonix, Inc. *The Electromagnetic Spectrum*. 15 Dec. 2007 <http://www.advancedphotonix.com/ap_products/terahertz_what_is.asp>.
- [44] A. G. Davies and E. H. Linfield, "Bridging the terahertz gap," *Phys. World* **14**, 37-41 (2004).
- [45] P. W. Kruse, "Principles of uncooled infrared focal plane arrays," in *Semiconductors and Semimetals 47: Uncooled Infrared Imaging Arrays and Systems*, P. W. Kruse and D. D. Skatrud, ed. (Academic Press, San Diego, 1997).
- [46] M. Tonouchi, "Cutting edge terahertz technology," *Nature Photonics* **1**, 97-105 (2007).
- [47] R. F. Kazarinov and R. A. Suris, "Possibility of amplification of electromagnetic waves in a semiconductor with a superlattice," *Fizika I Tekhnika Poluprovodnikov* **5**, 797-800 (1971).
- [48] J. Faist, F. Capasso, D. L. Sivco, C. Sirtori, A. L. Hutchinson, and A. Y. Cho, "Quantum cascade laser," *Science* **264**, 553-556 (1994).
- [49] F. Capasso, C. Gmachl, D. L. Sivco, and A. Y. Cho, "Quantum cascade lasers," *Physics World*, June 1999.

- [50] J. Faist, L. Ajili, G. Scalari, M. Giovannini, M. Beck, M. Rochat, H. Beere, A. G. Davies, E. H. Linfield & D. Ritchie, "Terahertz quantum cascade lasers," *Phil. Trans. R. Soc. Lond.* **362**, 215-231 (2003).
- [51] D. R. Chamberlin, P. R. Robrish, W. R. Trutna, G. Scalari, M. Giovannini, L. Ajili, and J. Faist, "Imaging at 3.4 THz with a quantum-cascade laser," *Appl. Opt.* **44**, 121-125 (2005).
- [52] D. J. Paul, University of Cambridge, *Si/SiGe Quantum Cascade Lasers*. 15 Dec 2007 <http://www.sp.phy.cam.ac.uk/~SiGe/QCL.html>>.
- [53] D. R. Chamberlin, "Imaging at 3.4 THz with a quantum cascade laser," presented at *Photonics West 2004: Integrated Optoelectronic Devices* (24 January 2004, San Jose, CA, USA).
- [54] Infrared Solutions, Inc. IR-160 Thermal Imager product information sheet (2004).
- [55] R. A. Wood, "Monolithic silicon microbolometer arrays," in *Semiconductors and Semimetals 47: Uncooled Infrared Imaging Arrays and Systems*, P. W. Kruse and D. D. Skatrud, ed. (Academic Press, San Diego, 1997).
- [56] Y. Lu, M. Hu, M. Wu, and Z. Liu, "Preparation of vanadium oxide thin films with high temperature coefficient of resistance by facing targets d.c. reactive sputtering and annealing process, *Surface & Coatings Tech.* **201**, 4969-4972 (2007).
- [57] E. L. Dereniak and S. D. Boreman, *Infrared Detectors and Systems*, Wiley, New York, 1996.
- [58] J. E. Schaar, K. L. Vodopyanov, and M. M. Fejer, "Intracavity terahertz-wave generation in a synchronously pumped optical parametric oscillator using quasi-phase-matched GaAs," *Opt. Lett.* **32**, 1284-1286 (2007).
- [59] University of California, Santa Barbara. *The UCSB FIR-FEL*. 15 Dec. 2007 <<http://sbfel3.ucsb.edu>>.
- [60] D. M. Wolfe, *A THz Micromagnetron*, M.S. thesis, Naval Postgraduate School, June 2006.
- [61] C. L. Tan, *MEMS-Based Terahertz Micromagnetron*, M.S. thesis, Naval Postgraduate School, Dec. 2007.
- [62] R. H. Giles, A.J. Gatesman, J. Fitzgerald, S. Fisk, and J. Waldman, "Tailoring artificial dielectric materials at terahertz frequencies," in the *Proc. 4th Intl. Syrup. Space THz Tech.*, Los Angeles, CA, April 1993.

- [63] R. H. Giles, A. J. Gatesman, and J. Waldman, "A study of the far-infrared optical properties of Rexolite™," *Int. J. Infrared and Millimeter Waves*, **11**, 1299 (1990).
- [64] A. J. Gatesman, R. H. Giles, and J. Waldman, "Submillimeter optical properties of hexagonal boron nitride," *Proc. of MRS Society* 242, 623 (1992).
- [65] A. J. Gatesman, A. Danylov, T. M. Goyette, J. C. Dickinson, R. H. Giles, W. Goodhue, J. Waldman, W. E. Nixon, and W. Hoen, "Terahertz behavior of optical components and common materials," *Proc. SPIE* **6212**, 62120E (2006).

INITIAL DISTRIBUTION LIST

1. Defense Technical Information Center
Ft. Belvoir, Virginia
2. Dudley Knox Library
Naval Postgraduate School
Monterey, California